A&A 407, 869–888 (2003)
DOI: 10.1051/0004-6361:20031026

Astronomy & Astrophysics

GaBoDS: The Garching-Bonn Deep Survey

I. Anatomy of galaxy clusters in the background of NGC 300⋆

M. Schirmer[1,2], T. Erben[1], P. Schneider[1], G. Pietrzynski[3,4], W. Gieren[3], S. Carpano[5], A. Micol[6], and F. Pierfederici[7,6]

[1] Institut für Astrophysik und Extraterrestrische Forschung (IAEF), Universität Bonn, Auf dem Hügel 71, 53121 Bonn, Germany
[2] Max-Planck-Institut für Astrophysik, Karl-Schwarzschild-Strasse 2, 85748 Garching, Germany
[3] Universidad de Concepción, Grupo de Astronomia, Casilla 160-C, Concepción, Chile
[4] Warsaw University Observatory, Al. Ujazdowskie 4, 00-478 Warsaw, Poland
[5] Institut für Astronomie und Astrophysik, Universität Tübingen, Sand 1, 72076 Tübingen, Germany
[6] Space Telescope European Coordinating Facility, Karl-Schwarzschild-Strasse 1, 85748 Garching, Germany
[7] National Optical Astronomy Observatory, 950 North Cherry Avenue, Tucson, USA

Received 13 May 2003 / Accepted 27 June 2003

Abstract. The Garching-Bonn Deep Survey (GaBoDS) is a virtual 12 square degree cosmic shear and cluster lensing survey, conducted with the WFI@2.2 m MPG/ESO telescope at La Silla. It consists of shallow, medium and deep random fields taken in *R*-band in subarcsecond seeing conditions at high galactic latitude. A substantial amount of the data was taken from the ESO archive, by means of a dedicated ASTROVIRTEL program.
In the present work we describe the main characteristics and scientific goals of GaBoDS. Our strategy for mining the ESO data archive is introduced, and we comment on the Wide Field Imager data reduction as well. In the second half of the paper we report on clusters of galaxies found in the background of NGC 300, a random archival field. We use weak gravitational lensing and the red cluster sequence method for the selection of these objects. Two of the clusters found were previously known and already confirmed by spectroscopy. Based on the available data we show that there is significant evidence for substructure in one of the clusters, and an increasing fraction of blue galaxies towards larger cluster radii. Two other mass peaks detected by our weak lensing technique coincide with red clumps of galaxies. We estimate their redshifts and masses, and check for possible X-ray counterparts in deep *XMM* observations.

Key words. cosmology: miscellaneous – galaxies: clusters: general – astronomical data bases: miscellaneous – gravitational lensing

1. Introduction

Light bundles from distant background sources are distorted by the tidal gravitational fields of the intervening matter distributed along the line of sight. This *shear* can be statistically measured by determining the image ellipticities of those background sources. Since it is linearly related to the underlying matter distribution, the shear can be used to measure statistical properties of the large-scale structure in the Universe (*cosmic shear*). It can also be used to detect clusters of galaxies, without assuming any hydrostatic equilibrium, symmetry or relation between luminous and dark matter. For recent reviews about weak gravitational lensing see Mellier (1999), and Bartelmann & Schneider (2001).

The amplitude of the distortions induced into galaxy images is of the order of a few percent for lensing by large-scale structure, and up to ten percent in the case of cluster lensing, depending on the mass of the cluster under consideration. The intrinsic ellipticities of galaxy images dominate the noise of the shear signal. Thus, a weak lensing analysis requires deep data with good PSF properties in order to measure enough galaxy ellipticities with sufficient accuracy. A large field of view and independent lines of sight guarantee a representative view of the universe, beating down the effect of cosmic variance. Deep wide field surveys provide this kind of data.

The Garching-Bonn Deep Survey (hereafter: GaBoDS) is a mostly virtual survey and covers a sky area of more than 12 square degrees with the Wide Field Imager[1] at the MPG/ESO 2.2 m telescope. Compared to other telescopes

Send offprint requests to: M. Schirmer,
e-mail: mischa@astro.uni-bonn.de

⋆ Based on observations made with ESO Telescopes at the La Silla Observatory.

[1] Hereafter we will use the term “WFI” for any Wide Field Imager instrument, and “WFI@2.2” when refering to the Wide Field Imager at the MPG/ESO 2.2 m telescope.

(VLT, CFHT, CTIO, WHT, KPNO) that have been successfully used for cosmic shear surveys so far (Bacon et al. 2000, 2002; Maoli et al. 2001; Kaiser et al. 2000; van Waerbeke et al. 2000, 2001; Wittman et al. 2000), the 2.2 m telescope is small in size, yet it offers an outstanding image quality. It allows for an independent confirmation of previously obtained results, and the detection of possibly remaining systematics in the data as well as in the measurement process.

In this paper we use weak gravitational lensing to detect dark matter haloes by looking for coherent shear patterns in galaxy images (Schneider 1996). In this manner galaxy clusters are detected directly relying on their most fundamental property, their mass, which is independent of their dynamical state and luminosity. Since structure formation in the Universe is highly sensitive to the cosmological model, shear-selected samples of dark matter haloes will yield new insights into the process of cluster formation (see Erben et al. 2000; Margoniner et al. 2003; Miyazaki et al. 2002; Dahle et al. 2002; Wittman et al. 2001, 2002, for shear-selected haloes). Based on simulations of the large-scale structure (Jain & van Waerbeke 2000) as well as on predictions from Press-Schechter models (Kruse & Schneider 2000) one expects some 10 shear-selected dark matter haloes per square degree. Therefore, the number of mass peaks in the GaBoDS data is expected to be of the order of 100. The mass of these peaks strongly depends on their redshift, as is shown in Sect. 5.

This work is organized as follows. In Sect. 2 we discuss our strategy for data mining the ESO archive. An outline of the main characteristics of the GaBoDS fields follows in Sect. 3, together with a compact overview of our WFI data reduction process in Sect. 4. Subsequently we report on the detection of galaxy clusters by means of weak lensing and the red cluster sequence method (Gladder & Yee 2000) in the NGC 300 GaBoDS field, and give a more detailed analysis for one of the clusters therein. We conclude in Sect. 6.

2. Data mining the ESO archive

2.1. Our ASTROVIRTEL program

For the above mentioned weak lensing analysis we aimed for a sky coverage of at least 10 square degrees for GaBoDS. Only about 3 square degrees were finally observed, however, in 20 allocated nights of our own GO program due to unfavourable weather conditions. Including available data from the EIS[2] Deep Public Survey and COMBO-17[3] left us with about 4 missing square degrees. A manual search in the large ESO archive turned out to be unfeasible, since the search engine available at that time did not allow filtering the data with respect to our requirements. The only usable fields we knew beforehand in the archive were the ones from the Deep Public Survey and one pointing of the Capodimonte Deep Field. Other WFI@2.2 data such as the five COMBO-17 fields were taken during MPG time before the 2.2 m telescope started into service mode operation, and were thus not publicly available through the archive. Besides, the very low number[4] of publications based on data taken with WFI@2.2 did not allow a direct identification of further usable data. We therefore proposed an ASTROVIRTEL program[5,6], aiming at an enhancement of the *querator*[7] search engine's capabilities (Pierfederici 2001). In order for a field to be included in the GaBoDS, the following requirements addressed by *querator* had to be met:

- minimum exposure time in R-band: $\sim$5 ksec,
- *image* seeing $\leq 1\farcs0$,
- random, at high galactic latitude,
- *empty*, i.e. avoidance of known very massive structures in or next to the field, no bright stars or large foreground objects inside the field.

The first item in this list guarantees a high enough number density ($\geq$10 arcmin^{-2}) of galaxies with securely measurable shapes. Furthermore, exposures must be taken in excellent seeing conditions, since the S/N for shape measurements decreases with the second power of the size of the PSF. The random character of the fields is needed to avoid a biasing towards certain types of objects, such as quasars or clusters of galaxies. In addition, it is ensured in this way that the fields sparsely sample the Universe along independent lines of sight, thus keeping the effect of cosmic variance small. The last point in the above item list is to further guarantee that a given pointing is usable for our purposes: massive structures such as large clusters of galaxies bias the search for unknown dark matter haloes as well as the measurement of a cosmic shear signal, which is about one order of magnitude smaller than the weak lensing signal of a large cluster. We are aware of the fact that this introduces a bias towards lower density lines of sight. By avoiding bright and large foreground objects we keep the usable area of an image as large as possible.

2.2. About data quality

It is clear that "data quality" is a very ambiguous term, highly dependent on the science which is to be drawn from the data. Given the involved and time consuming reduction of WFI data, we wanted to assess as best as possible the quality of archival data before any request or data reduction. This is straight forward for items such as the total exposure time, available filters, presence of bright objects, availability of calibration frames, and the ambient conditions during which the observation were performed (moon; clouds; seeing, according to the seeing monitor). However, not all of those can be expressed in terms of numbers; some judgement has to be done upon visual inspection of the data. Other data quality issues, such as image seeing or PSF properties can not be evaluated without more complex operations on the data itself. To address most of these points,

[2] ESO Imaging Survey.

[3] MPIA Heidelberg.

[4] Only about a dozen papers based on WFI@2.2 data have been published up to April 2002.

[5] ASTROVIRTEL cycle 2: Erben et al., *Gravitational lensing studies in randomly distributed, high galactic latitude fields.*

[6] `http://www.stecf.org/astrovirtel`

[7] `http://archive.eso.org/querator`

Table 1. Fields identified by our ASTROVIRTEL program. The second column gives the exposure time that went into the coaddition (images with very bad PSF or seeing were rejected). Exposure times in parentheses indicate the total exposure time per association as identified by *querator*.

Target	Exposure time	Image seeing
B08p3	4900 (5600)	0.″88
B08p2	4900 (5600)	0.″88
B08p1	4500 (5600)	0.″88
B0800	7200 (8300)	0.″88
B08m1	4500 (6000)	0.″88
B08m2	4000 (5800)	0.″88
B08m3	5400 (6000)	0.″96
Pal3	5000 (6120)	1.″0
AM1	7500 (7620)	1.″0
Comparison1	5300 (9300)	0.″97
C04p1	4000 (5600)	0.″88
C04p3	4000 (5600)	0.″83
C04m2	4000 (4800)	0.″85
C04m3	4000 (4800)	0.″85
NGC 300	15 100 (≈25 000)	1.″06
C04p2	4000 (5600)	0.″86
C04m1	4000 (4800)	0.″86
C04m4	4000 (4800)	0.″86
C0400	4800 (5600)	0.″87

the following demands were defined to ASTROVIRTEL and *querator*:

- measure the image seeing for all archived WFI@2.2 data,
- provide a preview facility, allowing quick visual inspection of the data ahead of a request,
- make available the corresponding proposal abstract ("why was this particular observation done?").

All but the last item were implemented. The image seeing, crucial for a weak lensing analysis, was determined by automatically extracting all non-saturated stars from one of the eight WFI@2.2 chips, and averaging their FWHM. It was superior to the DIMM[8] seeing, since the DIMM on La Silla could not pick up local effects such as dome seeing, zenith distance, flexure and temperature of the telescope's Serrurier structure, focus and tracking. On average we found the DIMM seeing to be 0.″1–0.″2 better than the image seeing for WFI@2.2. It was only in rare cases that the difference between the two drops below 0.″1.

In this way a list of useful candidate fields was extracted from the archive, minimizing the amount of unusable data slipping into the reduction process. Fields that were rejected at this late step suffered from scattered light or had very bad PSF properties[9]. Checking for PSF anisotropies in an image was very time consuming and thus not blindly performed on all data in the archive.

[8] Difference Image Motion Monitor.

[9] The anisotropy threshold depends on the overall quality of a particular data set. In general we rejected exposures with anisotropies larger than ∼6%.

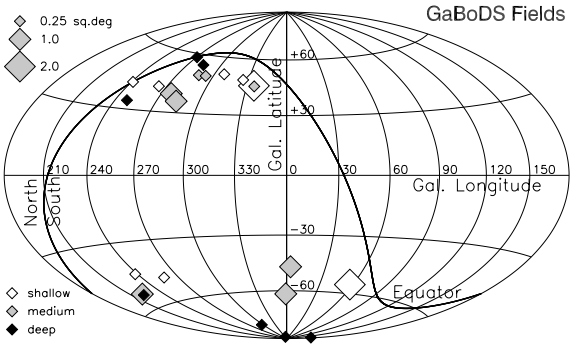

Fig. 1. Sky distribution of the GaBoDS fields. The size of the symbols depicts the covered sky area. All fields are at high galactic latitude.

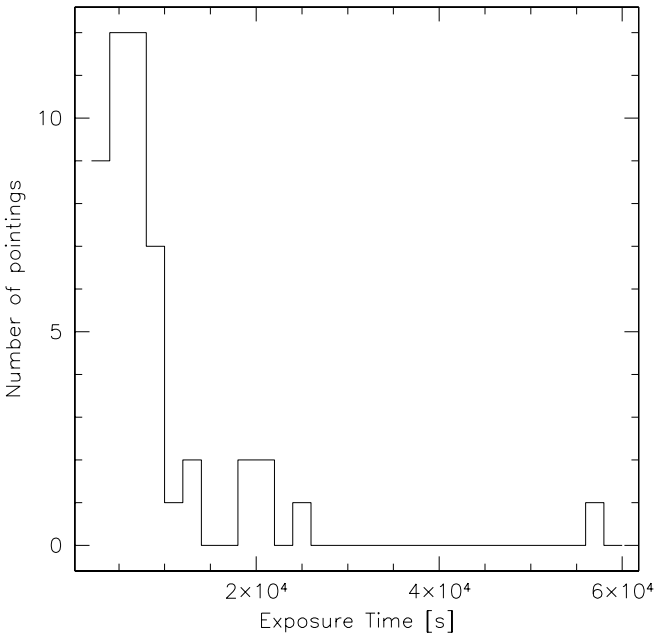

Fig. 2. Exposure times in GaBoDS. The peak at 56 ksec represents the Chandra Deep Field South (CDF-S).

Using the enhanced *querator* we found about 5 square degrees (20 pointings) of data in the ESO archive which satisfied our criteria, not counting the already known fields such as the ones from the EIS Deep Public Survey. This was twice the area we expected, but it must be noted that 15 of the pointings were done by a single observer, searching for trans-neptunian objects. The efficiency of our archive search with *querator* was about 75%, i.e. three out of four candidate fields were usable. Table 1 lists the fields found together with their image seeing.

3. Main characteristics of the GaBoDS fields

Since we made heavy use of archival data, we were able to collect more than 12 square degrees of high quality *R*-band images with only 10 clear nights of own observations. For nearly half of the fields multicolour information is also available. As can be seen from Figs. 1 and 2, the GaBoDS fields can be split into a shallow part (6 square degrees, 4–7 ksec total exposure time), a medium deep part (4.25 square degrees, 8–11 ksec) and a deep part (2.0 square degrees, 13–56 ksec). The survey fields

Table 2. GaBoDS data that was not taken by ourselves.

Sky coverage	Data source, depth of field
1.75 deg^2	ESO Imaging Survey + GOODS (medium, one deep)
5.00 deg^2	ASTROVIRTEL (mostly shallow, one deep)
1.25 deg^2	COMBO-17 survey (deep)
1.25 deg^2	ESO distant cluster survey (shallow, medium)
0.25 deg^2	NTT Deep Field, from the IR group at the MPI für extraterrestrische Physik (deep)
0.25 deg^2	Capodimonte Deep Field (deep)

are randomly distributed at high galactic latitude in the southern sky. Data in GaBoDS that was not taken by ourselves is summarised in Table 2. The image seeing in the stacked images is equal to or better than 1.″0, and our astrometric solution is accurate enough not to introduce artificial PSF anisotropies (see Sect. 4 for more details). The typical PSF quality of a stacked set of WFI@2.2 exposures in our survey can be seen in the lower right panel of Fig. 3. There we show the PSF anisotropies of a coadded image consisting of 57 exposures, giving a total integration time of 27.1 ksec. The image seeing of this particular field is 0.″8, thus possible shortcomings in the astrometric algorithm could easily be seen. The rms PSF anisotropy merely amounts to 0.8%, making WFI@2.2 very well suitable for weak gravitational lensing studies. The larger anisotropies in the field corners, especially in the lower left, are due to slightly tilted CCDs with respect to the focal plane (K. Meisenheimer, private communication). Optical abberations play only a minor role for this instrument.

Such quality of the data can only be achieved with a very carefully and frequently refocused telescope. The effect of a slightly defocused telescope on the PSF is shown in the remaining three panels of Fig. 3. One can see that anisotropies become significant once the detector is out of focus. Furthermore, the PSF rotates by 90 degrees when one passes through the focal plane. This is characteristic for tangential and sagittal astigmatism. Still the PSF of WFI@2.2 is very homogeneous over the field of view, even when crossing chip borders. Thus larger dither patterns can be used for the observations, and a single smooth model can be fitted to the PSF in the stacked mosaic (see also Fig. 6 in Sect. 5).

4. The art of WFI data reduction

4.1. The GaBoDS pipeline

The advent of multichip CCD cameras imposes new, high demands on data reduction. Pre-processing steps such as debiasing or flatfielding can be done independently on a chip-by-chip basis, allowing for efficient parallel processing on a multi-processor machine with sufficient disk space. Whereas these steps can be tackled using the same well-known algorithms as for single chip cameras, an accurate astrometric and photometric calibration of WFI data requires techniques going well beyond those routines. Different sensitivities of the CCDs and gaps between them lead to a very inhomogeneous exposure time and accordingly noise in the coaddition. An accurate weighting scheme is essential in order to retain control over these effects in the stacked image. In the following we describe our approach to WFI data reduction.

An almost fully automatic pipeline for WFI reduction was developed, based on existing software modules wherever possible, such as *EIS drizzle*[10], the Terapix[11] software suite, *FLIPS*[12] (J.-C. Cuillandre, not yet publicly available), *Eclipse*[13], *Imcat*[14] (N. Kaiser) and *LDAC*[15] (E. Deul, Leiden Data Analysis Center) (catalogue format and handling). *IRAF* was not used in the pipeline, apart from the drizzle coaddition, since it did not allow efficient scripting and reduction of this specific kind of data. A number of bash shell scripts were wrapped around those tools (mostly stand-alone C programs), allowing for an efficient, flexible and almost fully automatized end-to-end reduction of WFI data in parallel mode. The usage of the pipeline is not restricted to the WFI@2.2, but data from other instruments such as FORS1/2@VLT, ISAAC@VLT, SUPRIMECAM@SUBARU, MOSAIC-I@CTIO, MOSAIC-II@KPNO and WFI@AAO has already been successfully reduced. Supported architectures are Solaris, AIX, Linux and Dec-Alpha. The package will be released together with a detailed technical description (Erben et al., in preparation).

Our pipeline was designed with the GaBoDS data in mind, i.e. empty fields at high galactic latitude, with a fairly large dither pattern of up to 3.′0, and a very large number of single exposures per pointing. Still, the usage of the GaBoDS pipeline is not resticted to empty fields only. This is shown in Sect. 5, where we present an analysis of galaxy clusters behind NGC 300.

4.2. The pre-processing

Overscan correction, debiasing, flat fielding: apart from the astrometric, photometric and coaddition processes, all chips are processed individually, allowing for an easy parallelization of the code.

During pre-reduction, any instrumental signatures present in the data are removed. This includes overscan correction, bias subtraction and flat fielding with skyflats[16]. For the master biases all bias frames are median combined with outlier rejection. Flat fields are combined in the same way, but each flat exposure is normalised to 1 before the combination. Thus the different gains in the science images are still present after the flat fielding step. This is because we found that the chip-to-chip gain variations can be better determined from a superflat, which is drawn from already flatfielded exposures.

[10] http://www.eso.org/science/eis
[11] http://terapix.iap.fr
[12] http://www.cfht.hawaii.edu/~jcc/Flips/flips.html
[13] http://www.eso.org/projects/aot/eclipse
[14] http://www.ifa.hawaii.edu/~kaiser/imcat
[15] ftp://ftp.strw.leidenuniv.nl/pub/ldac/software
[16] For WFI@2.2 m telescope dome flats are inferior compared to skyflats.

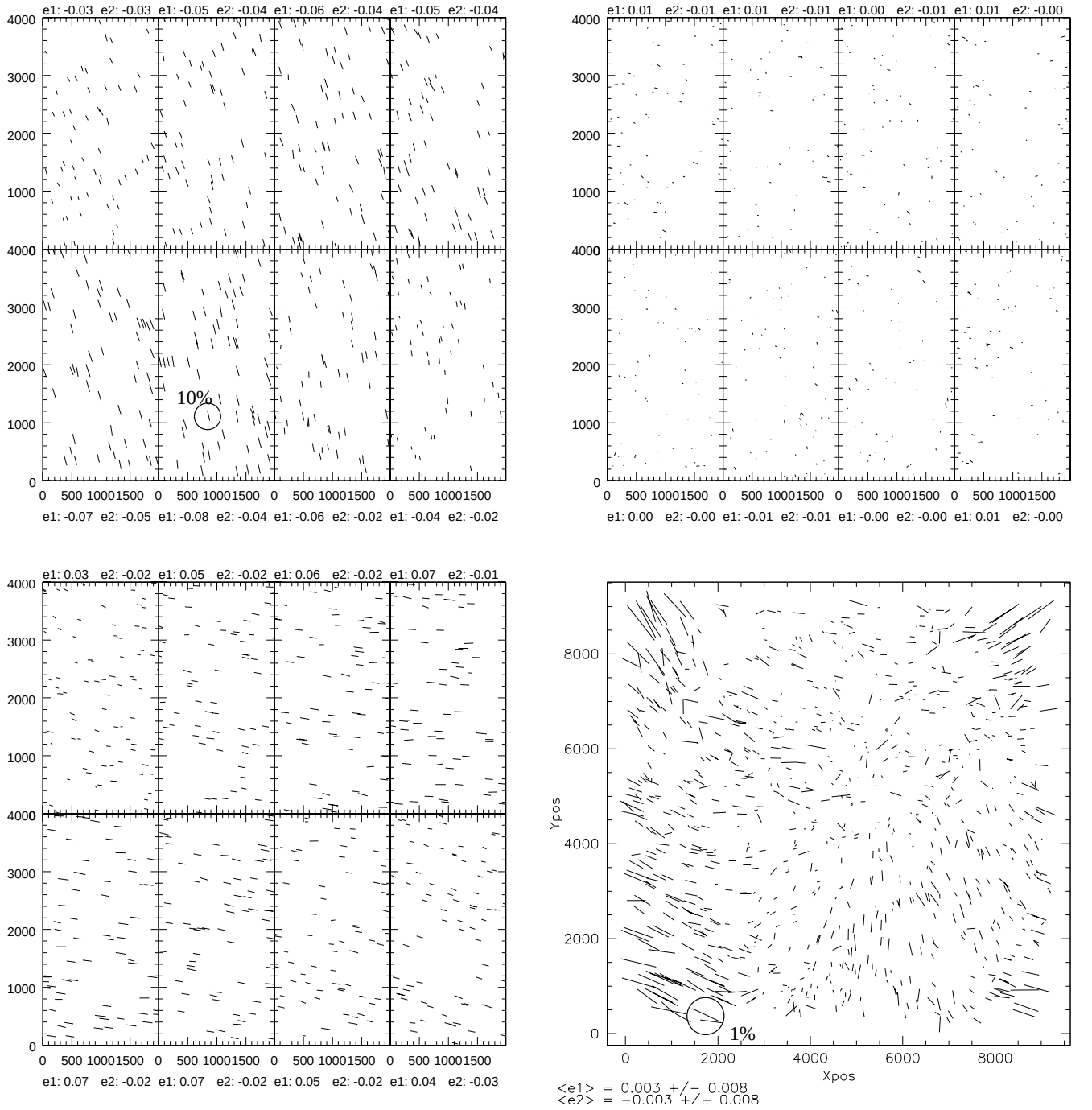

Fig. 3. PSF anisotropies for an intrafocal (upper left), focal (upper right) and extrafocal (lower left) exposure. The chosen scale for the stick length is the same for those three plots in order to show the increase in the anisotropies with respect to the focused exposure. The mean stellar ellipticities are 6.6%, 0.9% and 5.9%, respectively. The lower right panel depicts typical PSF anisotropies of a stacked WFI@2.2 *R*-band image (∼50 exposures with ∼500 s exposure time each). Note that the largest PSF anisotropy in the stacked image is as small as 0.8%. Compared to the other three PSF plots a different scale for the stick length was used in order to clearly show the anisotropies.

Creation of a superflat: residuals of around 3–4% after normal flat fielding are common for WFI@2.2 m, depending on sky brightness and the filter in use. A superflat is computed for correction of this effect, by median combining all images from a given observing run, using outlier rejection. Pixels that are affected by stars or galaxies are detected with *SExtractor* (Bertin & Arnouts 1996) and masked beforehand. In doing so we prevent the bright extended haloes around stars contributing to the superflat. The image constructed this way is then heavily smoothed, yielding an illumination correction image for every chip. All images are divided by their individual illumination correction. They are also normalised to the same (the highest) gain, which is accurately determined by comparing the modes of the individual superflats. Remaining residuals in the sky background are typically below 2%, and in the case of absence of bright stars, even below 1%.

Defringing: besides the illumination correction a fringing model is calculated by subtracting the illumination correction

from the previous superflat. Hereby it is assumed[17] that the amplitudes of the observed fringes scale directly with the sky background. The fringing model is then individually scaled for each image and subtracted. Fringing in the *R*-band is of the order of a few percent for WFI@2.2. Its correction makes sense only if more than ~10 images were used in the calculation of the model. Otherwise the pixel-to-pixel noise in the fringing model is larger than the fringing amplitude itself. This would introduce more noise into the individual defringed images than what is taken out by the correction of the lower frequency fringes. Since we are interested in measuring shapes of faint and small galaxies we want to avoid additional pixel-to-pixel noise. However, all images in the GaBoDS survey were constructed from many more than just 10 images, thus the contribution of additional high frequency noise is small, and we profit from taking out the gentle fringing pattern. In the case of the redder *I*-band the fringing can be much more prominent, and is in general more difficult to remove.

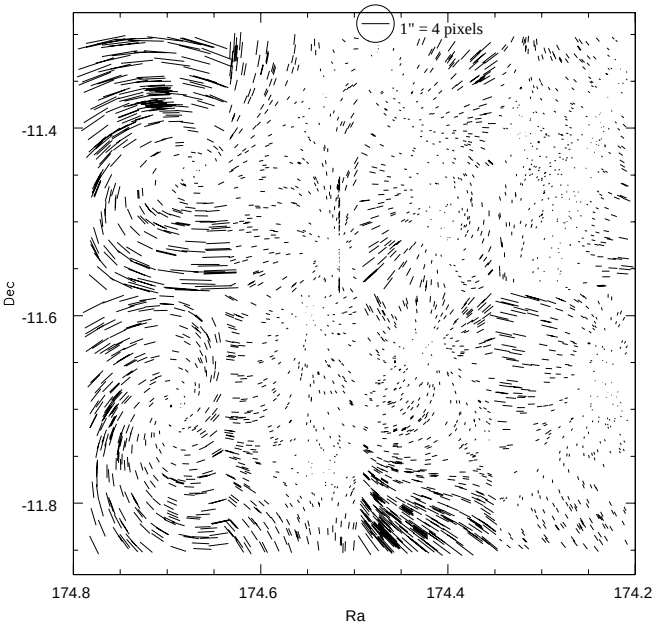

Fig. 4. Difference in object position between a single-shift approach and a full two-dimensional second order astrometric solution for the WFI@2.2. In other words, shown are the higher order terms needed for matching the CCDs to the sky. The patterns belonging to the left two chips are due to a rotation with respect to the mosaic. The maximum position difference in the plot is about six pixels, still a fairly small value compared to other telescope designs. It becomes clear that a single, global distortion polynomial for all CCDs does not work. Instead, every CCD has to be treated individually.

4.3. Astrometric calibration

After the pre-processing a global astrometric solution and a global relative photometric solution is calculated for all images. This is where the reduction of WFI data becomes much more complicated than the one for single chip cameras.

In the first step, high S/N objects in each image are detected by *SExtractor*, and a catalogue of non-saturated stars is generated. Based on a comparison with the USNO-A2 astrometric reference catalogue, a zero-order, single shift astrometric solution is calculated for each chip in every exposure. For a single-chip camera with a small field of view such an approach is often sufficient, but it no longer holds for multiple chip cameras with a large field of view. CCDs can be rotated with respect to each other, tilted against the focal plane, and in general cover areas at a distance from the optical axis, where field distortions become prominent[18]. Figure 4 shows the difference between a zero order (single shift with respect to a reference catalogue) and a full astrometric second order solution per CCD. From this figure it is obvious that the simple shift-and-add approach will not work for the whole mosaic. The issue is further complicated by the gaps between the CCDs and large dither patterns that are used to cover them. Thus, chips with very different distortions overlap. In addition, due to the large field of view, the observed patch of the sky must no longer be treated as a flat plane, but as a spherical curved surface.

In the second step we use Mario Radovich's *Astrometrix*[19] (Terapix) package to fit third order polynomials to every chip in every exposure, in order to correct for the above mentioned effects and to find a global astrometric solution. For this purpose all high S/N objects (stars and galaxies) detected in the first step are identified with each other, including those from the overlap regions. The latter ones are most important in establishing a global astrometric (and photometric) solution, since the accuracy of available reference catalogues such as the USNO-A2 (0.″2 rms) is insufficient for sub-pixel registration. Thus the astrometric solution is determined from the data itself. The USNO-A2 is used only to fix the solution with respect to absolute sky coordinates within 0.″2 rms. With *Astrometrix* we consistently achieve an internal astrometric accuracy of 1/20–1/10th of a pixel (0.″02–0.″01), thus the final PSF is mostly determined by the intrinsic PSFs of the single exposures (see Fig. 3). Additional, artificial seeing and PSF anisotropies are introduced into the stacked image on a very low level only, even for very large data sets such as the CDF-S, consisting of 150 WFI@2.2 R-band exposures. This is a crucial requirement for our weak lensing analysis.

4.4. Photometric calibration

Once an astrometric solution is found, a relative photometric solution is straight forward. Relative fluxes of objects in different exposures and overlap regions are compared, allowing the calculation of relative photometric zeropoints for every chip and every exposure. Given two overlapping chips k and j,

[17] This assumption only holds for photometric nights. In non-photometric nights it can be impossible to remove fringing in the *I*-band, since the model is changing within minutes on scales smaller than the field of view of a single CCD.

[18] A ZEMAX analysis (Philipp Keller, private communication) for the 2.2 m Ritchey Chretien telescope design and WFI@2.2's focal reducer shows that the radial field distortion for this layout increases with $\delta = a_1 r^2 + a_2 r^6$. However, the total amplitude of this distortion is very small (~30 pixels).

[19] `http://www.na.astro.it/~radovich/WIFIX/astrom.ps`

consider all $i = 1...N$ objects and calculate the mean deviation of magnitudes K and J

$$M_{k,j} := \frac{\Sigma_i W_i (K_i - J_i)}{\Sigma_i W_i}, \quad (1)$$

with $W_i = (\sigma_K^2 + \sigma_J^2)^{-1}$, where σ are the measurement errors of the corresponding magnitudes. Objects deviating in $K_i - J_i$ more than a user defined threshold are rejected. The relative zeropoints ZP_l for all $N_{\rm over}$ overlapping CCDs are determined by χ^2 minimization with respect to ZP_k:

$$\chi^2 = \sum_{k,j}^{N_{\rm over}} \left[M_{k,j} - (ZP_k - ZP_j) \right]^2 . \quad (2)$$

Finally, the relative zeropoints of photometric images are normalised so that their mean is zero. This approach assumes that the relative zeropoints are constant for every CCD[20]. An automatic absolute photometric solution is not yet implemented in the pipeline.

4.5. A statistically optimized weighting scheme

The effective exposure time for a stacked WFI mosaic is highly non-uniform. Read noise and the flatfields are chip-dependent, and gaps between the CCDs contribute further to the inhomogeneous depth of a stacked image. Applying a statistically optimized weighting scheme to the exposures during coaddition allows for a significantly improved object S/N ratio (up to a factor of ∼1.5).

We now describe our approach to assign an individual weight map for every science image. In a first step, a pixel is assigned its normalised skyflat value as a weight, which contains the information about relative gains between the CCDs and pixel-to-pixel sensitivities. Contrary to other methods, we do not detect 'bad' pixels (hot or cold pixels, pixels affected by cosmics, reflections or satellite tracks) by intercomparing all images in the stack, but on the individual images themselves. For the detection of permanent image defects, such as hot or dead pixels and bad columns, we use dark frames and superflat images. Affected pixels are set to zero in the corresponding weight map. Thus every chip in the WFI mosaic has its own basic weight map after the first step. Weight maps created in this way are the same for all exposures in a data set unless they were flatfielded with different skyflats or taken several weeks apart.

In a second step these weight images are adjusted individually for every image. Remaining hot pixels and cosmics are easily identified with *SExtractor* in conjunction with *Eye* (Terapix), since they appear much sharper than the stellar PSF even under good seeing conditions. Bright reflections and satellite tracks, however, need to be masked by hand, the only step in the pipeline which is not yet automatized. Moving objects like asteroids go unmasked and show up as dashed lines in the stacked image. During coaddition the individual weight maps are scaled with correction factors for airmass and varying photometric conditions. Changing seeing conditions from image to image can be included on an optional basis, too. All individual weight maps are resampled and coadded in exactly the same way as the respective science images, yielding the noise properties for all pixels in the final coadded image (see Fig. 5 for an example).

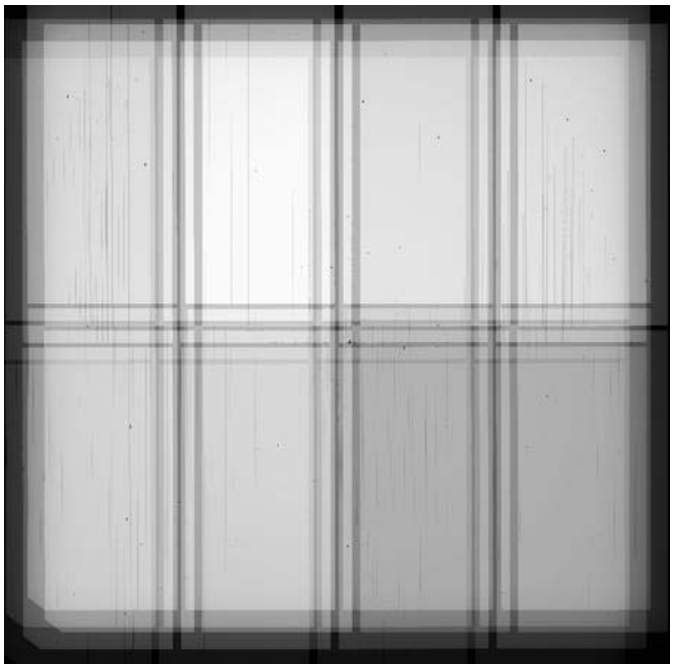

Fig. 5. Coadded weight image of a small WFI@2.2 data set consisting of five exposures. One clearly identifies regions with less effective exposure time due to gaps between CCDs and different pixel sensitivities. The size of the dither pattern also becomes obvious. Brighter regions correspond to pixels with higher weight. The variations from chip to chip are due to differences in the gain and the flatfield.

4.6. The coaddition process

Before the coaddition, all images are sky subtracted. In order to model the sky background we detect all objects in the field with *SExtractor* and replace them with the mean background as determined from the remaining pixels. This image is then convolved with a very broad smoothing kernel (width between 200 and 500 pixels) and subtracted from the science image itself.

For the coaddition the *EIS drizzle* in *IRAF* is used. It allows for a weighted mean coaddition, guaranteeing the best S/N in the stacked image. The resampling strategy ensures that the PSF is not artificially bloated in the stack, and that a varying pixel scale is correctly taken into account also from a photometric point of view. Alternatively, one can use *swarp* (E. Bertin, Terapix), which contrary to *drizzle*, makes use of much more advanced resampling algorithms and does not lead to correlated noise in the stacked image. However, the differences between *swarp* and *drizzle* vanish if many images are stacked, which is the case in GaBoDS.

Four factors determine the value of an output pixel in the coadded image. We have the input pixel value I_i from the science chip and an associated value W_i in the weight map. I_i represents the part of the input pixel that is mapped onto the

[20] Zeropoint variations for images taken with WFI@2.2 that were not superflat corrected are described in:
`http://www.ls.eso.org/lasilla/sciops/wfi/zeropoints`

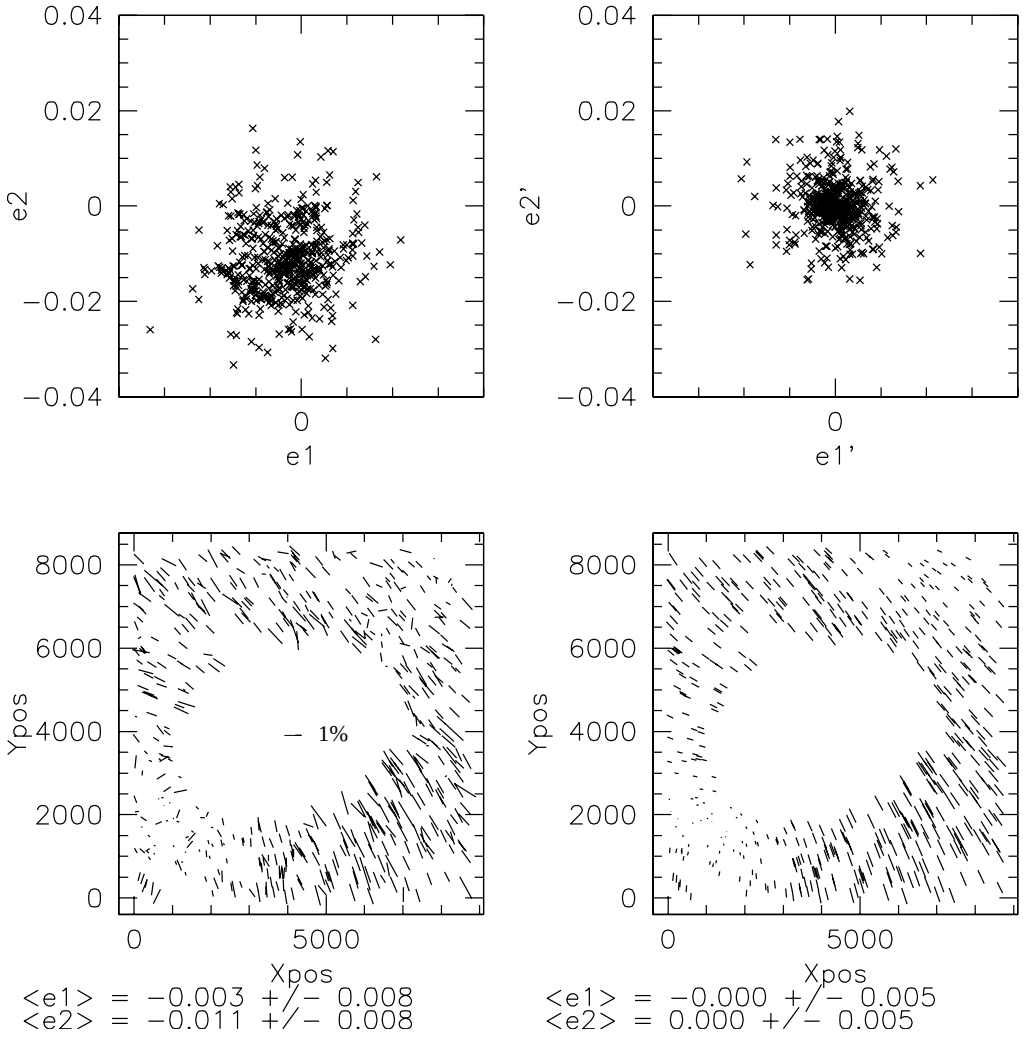

Fig. 6. PSF anisotropies in the NGC 300 *R*-band image. Upper left: before correction, upper right: after correction. Lower left: Anisotropies as measured in the image, lower right: a two-dimensional polynomial fit to the PSF anisotropies.

corresponding output pixel. Besides, I_i is scaled with factors f_i to the consistent photometric zeropoint and to a fixed exposure time (we chose 1 s for this purpose):

$$f_i = 10^{-0.4\,ZP_i}/t_i, \tag{3}$$

where t_i is the exposure time and ZP_i the relative photometric zeropoint. All images are also weighted according to their sky noise. This weight scale is given by:

$$w_i = \frac{1}{\sigma^2_{\mathrm{sky},i} f_i^2}. \tag{4}$$

Here we take into account the fact that the noise also scales with the flux scale f_i. The values I_{out} and W_{out} in a stack of N images then read

$$I_{\mathrm{out}} = \frac{\sum_{i=1}^{N} I_i f_i W_i w_i}{\sum_{i=1}^{N} W_i w_i}, \qquad W_{\mathrm{out}} = \sum_{i=1}^{N} W_i w_i. \tag{5}$$

EIS drizzle creates its output with the TAN projection. Alternatively, the COE projection can be used (see Greisen & Calabretta 2002, for further information on sky projections). In the stacked images North is up and East to the left. A reference coordinate can be specified for the coaddition. Thus, if multicolour information is available for a particular pointing, the stacked images in the different bands are automatically registered with subpixel accuracy.

5. Galaxy clusters in the background of NGC 300

5.1. Characteristics of the data

One of the ASTROVIRTEL fields was a deep multicolour observation of NGC 300 (see Table 1), a face-on spiral galaxy in the Sculptor group at a distance of about 2.1 Mpc (Freedman et al. 2001). Its angular size is $25' \times 18'$, occupying about 40% of the WFI@2.2 field of view ($34' \times 34'$). The field did thus not meet all requirements for GaBoDS, but the image seeing of a significant fraction of the *R*-band data was around $1\farcs0$. Deep *V*-band observations (∼37 ksec, $1\farcs13$ image seeing) were available too. This allowed us to search for distant galaxy clusters in the background of NGC 300 by means of weak lensing and the red cluster sequence method.

Upon visual inspection in the Digitized Sky Survey (DSS) before the data retrieval request, we recognized two concentrations of fainter galaxies north-east and south-east of NGC 300,

at the edge of the WFI@2.2 field. 21 spectra were taken for the first concentration by Cappi et al. (1998) (hereafter CHM98), confirming a cluster at redshift 0.165. The second, less prominent concentration is known as EDCC-499 at a redshift of 0.117 (Collins et al. 1995). Hereafter we refer to these clusters as CL0056.03–37.55 (CL0053–37 in CHM98) and CL0056.02–37.90, respectively, using their epoch 2000.0 equatorial coordinates. The WFI@2.2 data for NGC 300 was taken for the ARAUCARIA project (Pietrzynski et al. 2002a), an attempt to fine-tune the distance ladder by comparing different distance indicators such as cepheids, blue supergiants, tip of the red giant branch, and planetary nebulae for various nearby galaxies. Since NGC 300 was monitored in 34 nights between July 1999 and January 2000, the creation of deep multicolour images was feasible[21].

5.2. Data reduction and catalogue creation

The NGC 300 data was reduced essentially in the same way as described in Sect. 4. Due to the large extent of this galaxy a superflat could only be calculated for the field outside NGC 300. Pixels lying inside the galaxy were only corrected for the gain differences, which were determined from the unaffected outer area. The same held for the sky subtraction of individual images before the coaddition process. The sky was modeled outside NGC 300 and assumed to be constant inside, so that no discrete jumps appeared between the inner and outer part. This image was then smoothed with a large kernel and subtracted. A substantial part of the images suffered from secondary scattering light, and from occasional vignetting caused by the filter holder. Most affected was the south-eastern corner of the field, where CL0056.02 is located. Our analysis therefore mainly concentrates on CL0056.03.

The photometric zeropoint of the coadded V-band image was determined by matching stellar magnitudes to the secondary standard stars established by Pietrzynski et al. (2002b) in the Johnson-Cousins system. No calibration was available for the R-band, for which a zeropoint was determined based on the expected $V-R$ colour for the red sequence of CL0056.03 ($z = 0.165$). We estimate it to be accurate within $0\overset{\mathrm{m}}{.}1$, which is sufficient for the analysis presented here since it does not rely on highly accurate absolute photometry.

For the production of colour catalogues the coadded images were normalised so that their mean background noise $\sigma_{\mathrm{back}} = 1$. They were then coadded without further rescaling, yielding a high signal-to-noise detection image. For this stack an adapted weight map was created combining the individual weight images accordingly. For the creation of a colour catalogue we used the detection image, the detection weight map and the unnormalised images from filters V and R, as an input for *SExtractor*. Thus the flux for objects in different filters was measured within the same aperture, yielding relative colour information for galaxies with good internal accuracy. A further advantage of this approach was that the objects detected in the single catalogues for the V- and R-bands were already in the same order and easily merged into one colour catalogue. We calculated the galaxy colours from isophotal magnitudes (MAG_ISO), and used MAG_AUTO for the magnitudes themselves.

[21] A colour image made from this data set can be found at `http://www.eso.org/outreach/press-rel/pr-2002/phot-18a-02-hires.jpg`

5.3. Using weak shear for cluster detection

In the following standard weak lensing notations are used. For a technical review of this topic see Bartelmann & Schneider (2001). The tidal gravitational field of a cluster-sized mass concentration induces a coherent distortion pattern in the images of distant background galaxies. By scanning the field for such characteristic distortion patterns one can detect mass concentrations directly, irrespective of their luminosity (see Erben et al. 2000; Umetsu & Futamase 2000; Wittman et al. 2001; Miralles et al. 2002, for examples).

We use the *aperture mass statistics* M_{ap} (Schneider 1996) for the detection of galaxy clusters. M_{ap} is a filtered integral of the projected mass distribution, κ, inside an aperture. Its definition reads

$$M_{\mathrm{ap}} = \int_0^\theta \mathrm{d}^2\vartheta\, \kappa(\boldsymbol{\vartheta}, z_{\mathrm{d}}, z_{\mathrm{s}})\, U(\vartheta). \tag{6}$$

z_{d} and z_{s} are the lens and source redshifts, and $U(\vartheta)$ is a compensated filter, i.e. $\int_0^\theta d\vartheta\, \vartheta\, U(\vartheta) = 0$. The filter function $U(\vartheta)$ is chosen as

$$U(\vartheta) = \frac{9}{\pi\theta^2}\left(1-\left(\frac{\vartheta}{\theta}\right)^2\right)\left(\frac{1}{3}-\left(\frac{\vartheta}{\theta}\right)^2\right). \tag{7}$$

By defining the new filter function

$$Q(\vartheta) = \frac{2}{\vartheta^2}\int_0^\vartheta \mathrm{d}\vartheta'\vartheta' U(\vartheta') - U(\vartheta), \tag{8}$$

M_{ap} can be expressed in terms of the tangential shear γ_{t}, for which the observable ellipticities ϵ_{t} of the background galaxies are an unbiased estimator, as

$$M_{\mathrm{ap}} = \int_0^\theta \mathrm{d}^2\vartheta \gamma_{\mathrm{t}}(\boldsymbol{\vartheta}) Q(\vartheta) \approx \frac{1}{n}\sum_i \epsilon_{\mathrm{t}}(\boldsymbol{\vartheta}_i) Q(\vartheta_i). \tag{9}$$

Hence, we can calculate the scalar M_{ap} directly from observables. The noise for M_{ap} is evaluated as

$$\sigma^2_{\mathrm{Map}} = \frac{\pi\sigma_\epsilon^2}{n}\int_0^\theta \mathrm{d}\vartheta\,\vartheta\, Q^2(\vartheta) \rightarrow \frac{\sigma_\epsilon^2}{2n^2}\sum_i Q^2(\vartheta_i), \tag{10}$$

where σ_ϵ is the ellipticity dispersion and n the number density of background galaxies. We determined $n = 20$ arcmin^{-2} and $\sigma_\epsilon = 0.34$ for the WFI@2.2 data at hand. Based on this expression, the S/N ratio for mass peaks can be estimated. For doing so, a projected mass distribution $\kappa(\boldsymbol{\vartheta}, z_{\mathrm{d}}, z_{\mathrm{s}})$ at a redshift z_{d} is assumed, together with a redshift distribution $p(z_{\mathrm{s}})$ for the lensed galaxies. The expected signal S then reads

$$S = \int_0^\theta \mathrm{d}^2\vartheta \int_{z_{\mathrm{d}}}^\infty \mathrm{d}z_{\mathrm{s}}\, \kappa(\boldsymbol{\vartheta}, z_{\mathrm{d}}, z_{\mathrm{s}}) U(\vartheta) p(z_{\mathrm{s}}). \tag{11}$$

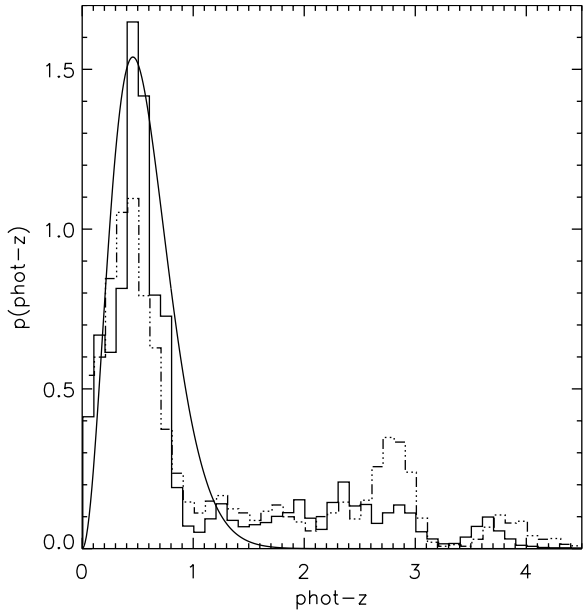

Fig. 7. Photometric redshift distribution for the Chandra Deep Field South, determined from *UBVRI* WFI@2.2 photometry. The redshifts were estimated with *hyperz* (solid line) (Bolzonella et al. 2000). Only objects that had a good redshift fit of $P(\chi^2) > 0.9$ went into the distribution shown. The dash-dotted line shows an independent measurement of the photometric redshifts from E. Hatziminaoglou (ESO) for the same data set (private communication). The peak at $z = 2.8$ is due to a degeneracy between low and high redshift galaxies and appeared since no prior for the luminosity of galaxies was used. These excess objects are randomly drawn from the low-z regime. Thus the main peak of this distribution was lowered, but not shifted in redshift. Equation (12) was fitted to both distributions, yielding consistent values $z_0 = 0.373$ (0.377).

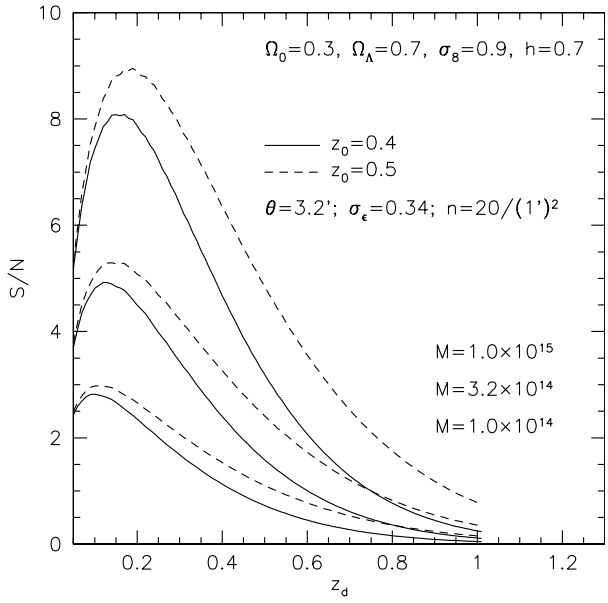

Fig. 8. The expected S/N ratios for various massive dark matter haloes, as detected with $M_{\rm ap}$ in the NGC 300 WFI@2.2 field. The effect of a background galaxy population with higher redshift is shown, too.

For the mass distribution a NFW profile (Navarro et al. 1996) was used. Kruse & Schneider (1999), showed how to convert this profile into the projected surface mass density, κ. For the source redshifts we took the normalised distribution

$$p(z_{\rm s}) = \frac{3}{2z_0}\left(\frac{z_{\rm s}}{z_0}\right)^2 \exp\left[-\left(\frac{z_{\rm s}}{z_0}\right)^{1.5}\right], \qquad (12)$$

proposed by Brainerd et al. (1996). We fixed the parameter z_0 based on photometric redshifts, computed from the *UBVRI* WFI@2.2 data (EIS Deep Public Survey) for the Chandra Deep Field South. The exposure time in the *R* filter was 9000 seconds, lower than the ∼15 000 s for the NGC 300 field. Figure 7 shows the photometric redshifts and the fit to the $p(z_{\rm s})$ profile. A value of $z_0 = 0.37$ is determined from the fit. We conservatively increased this value to $z_0 = 0.4$ for the S/N computation, given the significantly larger exposure time in *R*.

Figure 8 shows some predicted S/N ratios for massive haloes as a function of redshift. From this plot we see that clusters with masses of $3.2 \times 10^{14}\ M_\odot$ are detectable up to a redshift of $z = 0.35$ (0.42), and those with $1.0 \times 10^{15}\ M_\odot$ can be found up to $z = 0.5$ (0.65) for a filter size of 3.′2 (4.′0, not shown). We are not sensitive to structures with $\sim 1.0 \times 10^{14}\ M_\odot$ at the 3.′2 scale, but can detect them at the 4.′0 scale up to $z = 0.14$. For comparison, S/N ratios are also shown for the case when background galaxies are at somewhat higher redshift ($z_0 = 0.5$). The S/N ratio for $M_{\rm ap}$ peaks in a given data field can also be determined from the data itself, by randomizing ellipticities while keeping galaxy positions fixed. In the following we make use of this fact. For the weak lensing analysis the *R*-band image was used. To avoid any biasing of the detection algorithm, NGC 300 was masked and replaced by the mean sky background, removing most of the flux present in the image. With *SExtractor* all objects with at least 6 connected pixels $\geq 2\sigma$ above the sky background noise were detected. This catalogue contained 44 146 objects. The shear estimates for these objects were determined with the KSB algorithm as proposed by Kaiser et al. (1995). An extensive description of our approach using the KSB method, including the PSF corrections, can be found in Erben et al. (2001). Figure 6 shows the measured and the corrected PSF anisotropies for this particular field. After filtering, the background galaxy catalogue contained 12 694 objects with securely determined shapes, a detection significance $\nu > 12$ (calculated by KSB) and a bright magnitude limit of $R > 23.0$. This translates to the above mentioned number density of ∼20 galaxies per square arcmin.

Figure 9 shows the $M_{\rm ap}$ results for various filter widths. As can be seen, we recovered CL0056.03 in all but the largest filter scale at a 3σ level within 50–100″ south of the cluster centre, whereas CL0056.02 was not detected. For the latter cluster useful shear information could only be obtained from about 30% of the area which would be available if the cluster did not lie next to the field corner in a region with bad image quality. This increased the noise in $M_{\rm ap}$ by a factor of ∼3. The argument of field truncation also holds for CL0056.03, but to a much lesser extent. There the useable field was limited by the edge of the image, 2.′5 east of the cluster centre, and NGC 300 5.′5 southwest. From our previous S/N considerations we conclude that a

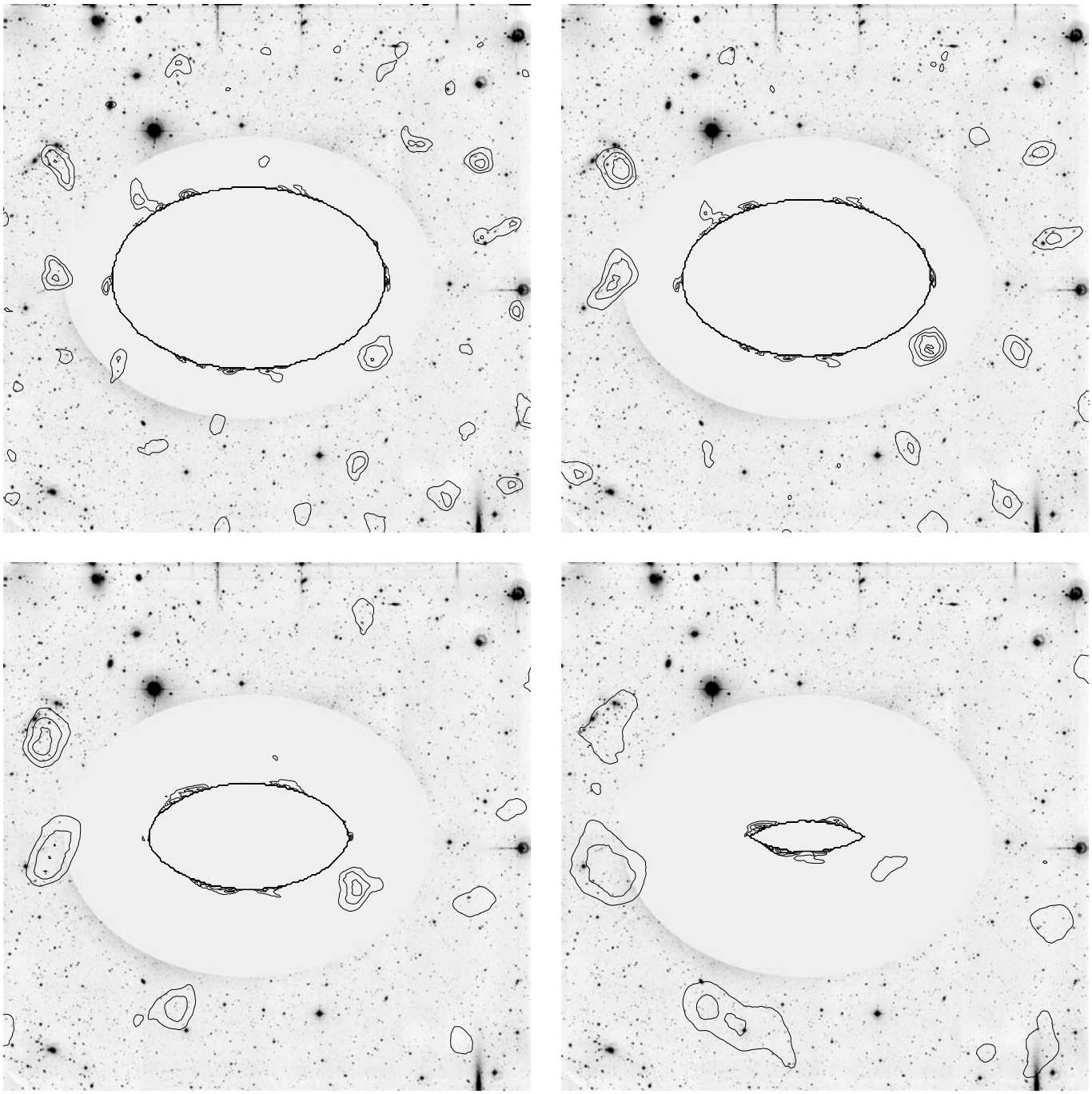

Fig. 9. The $M_{\rm ap}$ statistics for various filter scales: 3.′2 (upper left), 4.′0 (upper right), 5.′6 (lower left) and 8.′0 (lower right). Shown are $M_{\rm ap}$ probability contours drawn from 5000 randomisations each. The contours depict the 2.0, 2.5, 3.0, 3.5σ levels. The cluster CL0056.03 can be found left of the brightest star, and CL0056.02 sits in the lower left corner. See also Figs. 13 and 14 for comparison. The large elliptical contour arises from the fact that $M_{\rm ap}$ can not determine any value for the pixels inside the contour, since for those no galaxies lie inside the filter. Thus, the distance from this ellipse to the outer edge of the mask depicts the radius of the $M_{\rm ap}$ filter function.

mass of $\sim 1.4 \times 10^{14}\ M_\odot$ at redshift of $z = 0.165$ would produce a comparably significant $M_{\rm ap}$ detection.

The $M_{\rm ap}$ statistics furthermore picks up a number of other peaks. In the upper left panel of Fig. 9, the one for the smallest filter scale, we find a 3σ peak that drops to 2.5σ in the upper right panel, and vanishes for larger filter scales (clump "C"). Another peak below CL0056.03 is detected at the 3σ level for all but the largest filter scale (clump "A"). Both peaks lie within 50″ and 20–70″ of two clumps of red galaxies, as is shown in the next section. There we determine their redshifts $z_{\rm d,A} = 0.47$ and $z_{\rm d,C} = 0.43$. Our S/N calculations then yield masses of $M_{\rm A}(4.'0) \approx (4 \pm 3) \times 10^{14}\ M_\odot$ and $M_{\rm C}(3.'2) \approx (6 \pm 3) \times 10^{14}\ M_\odot$ for these two clumps and for the filter scales in which they are detected most significantly. See also Fig. 14 for those two concentrations of red galaxies.

Table 3. All clumps except "C" lie close to the peak of the track in Fig. 12, reducing the ambiguity in their redshift estimate.

Red clump	$\langle V-R\rangle$	$z_{\rm est}$
A	1.46 ± 0.02	0.47 ± 0.05
B	1.50 ± 0.03	0.47 ± 0.05
C	1.41 ± 0.02	$0.43 \pm 0.05, 0.51 \pm 0.05$
D	1.50 ± 0.03	0.47 ± 0.05

Besides, a stable peak is found inside the mask of NGC 300, with a detection limit of $3-3.5\sigma$ for the three smaller filter scales. Such a detection is not surprising, since $M_{\rm ap}$ is a highly non-local measure. It can pick up those parts of the shear field from a possible cluster hidden behind NGC 300 that extend beyond NGC 300 itself. Shear fields for massive clusters of galaxies have been traced beyond $10'$ of cluster centres (see Clowe & Schneider 2002, for examples), thus a sufficiently massive cluster behind NGC 300 could easily be picked up. The detection in question is at the very outer edge of the galaxy disk, but the confusion limit of foreground stars in NGC 300 is already reached. Yet the optical thickness of the disk is still small, so that three larger and brighter isolated galaxies can be seen within a $2'$ wide window. Thus, if there was a massive lower redshift cluster such as CL0056.03 at this position, it could be seen through the disk. There is no indication for such an object at this position. More distant clusters, however, could no longer be identified as such, since their smaller and fainter images are drowned in the foreground confusion.

5.4. X-ray observations of the NGC 300 field

No excess X-ray emission is found in the ROSAT All Sky Survey (Voges et al. 1999) for the $M_{\rm ap}$ detections, apart from CL0056.03. Nor do we find a X-ray counterpart for clump "A" in the source list of Read & Pietsch (2001), who observed the NGC 300 field for 46 ksec with ROSAT PSPC. Clump "C" is slightly outside the ROSAT field of view. A more recent and much deeper (100 ksec) observation by M. Turner in 2002 with XMM-Newton also misses clump "C", but picks up some diffuse emission from the fringes of CL0056.03. Clump "A" remains undetected at the very edge of XMM's field of view, where the total throughput of the system drops to 28% due to vignetting. See Fig. 10 for the XMM sources in the NGC 300 WFI field.

5.5. Using the red sequence for cluster detection

In a $(V-R, R)$ colour–magnitude diagram (Fig. 11), plotted for all galaxies in the vicinity of NGC 300, we loosely selected a red cluster sequence with $0.67 < V-R < 0.87, 13.0 < R < 21.0$. The sky distribution for objects inside this window is plotted in Fig. 13 (big red dots), whereas all other objects with $R < 21$ and outside the window are shown as small dots. We then calculated the rms of the projected density of all red sequence members, and overlaid isodensity sigma-contours for their distribution. The smoothing length for the density was $3\farcm6$. We recover CL0056.03 and CL0056.02 at the 8σ and 5σ level in overdensity, respectively. Thus the cluster sequence we selected in the colour–magnitude diagram is actually a merger of two clusters of galaxies.

The remaining galaxies that lay within the red sequence window, but which did not belong to either of the two clusters, did not clump throughout the rest of the field on a level higher than 1σ. Furthermore, all galaxies brighter than $R = 20$ and outside the red sequence window showed no clumping at a level higher than 2σ. We additionally checked the clustering properties of all objects brighter than $R = 23$, by moving a rectangular aperture over all relevant galaxies in the colour–magnitude distribution. We did not find any highly significant clumping apart from galaxies with $1.37 < V-R < 1.56, 19.0 < R < 22.5$. There we found four significant overdensities "A" to "D", with "A" and "C" coincident with $M_{\rm ap}$ detections (see above). Table 3 summarises the properties and redshift estimates based on the track for elliptical galaxies in Fig. 12. We see that all clumps lie at similar redshifts, with some ambiguity for clump "C". Actually, peaks "A" and "B" could form a connected system if spectroscopically confirmed to be at the same redshift. More details are given in the caption of Fig. 14.

5.6. Increasing fraction of blue galaxies towards larger cluster radii

Figure 15 depicts the two colour–magnitude diagrams for CL0056.03 and CL0056.02. Shown are galaxies with $V-R = 0.80 \pm 0.5$, $13.0 < R < 21.0$ and within $5\farcm5$ of the cluster centres. These galaxies were split into three distance bins (see Fig. 15), in order to detect a possible evolution in their colour as a function of distance from the cluster core. The number of interlopers is small; we counted 41 galaxies with the same properties in a $6\farcm5 \times 33'$ strip on the opposite side of NGC 300, corresponding to a number density of about 0.19 galaxies per square arcmin. If no further clumping takes place along the line-of-sight, 11% (19%) of interlopers can be expected within the area under consideration for CL0056.03 (CL0056.02).

For CL0056.03, in the innermost bin 11 out of 19 galaxies have measured redshifts, in the second bin it is 10 out of 60 galaxies, and in the outermost bin none of the 34 galaxies have known redshifts. 10 galaxies appear to lie above the upper envelope ($V-R > 0.87$) of the cluster sequence,7 of those are from the second distance bin, and the rest comes from the third bin. Their number is in agreement with the expected amount of interlopers. 4 of those 10 galaxies are spatially concentrated within $1\farcm2$. None of the 10 has spectroscopically determined redshifts, we assume that they are in the background of CL0056.03 since they lie beyond the upper envelope of $V-R < 0.87$ as defined by the red sequence.

A closer inspection of the colour–magnitude diagram for CL0056.03 reveals several features:

– Galaxies within 172 kpc of the cluster core (red dots) follow a tight correlation of

$$V-R = (-0.013 \pm 0.004)R + 1.028 \pm 0.077. \quad (13)$$

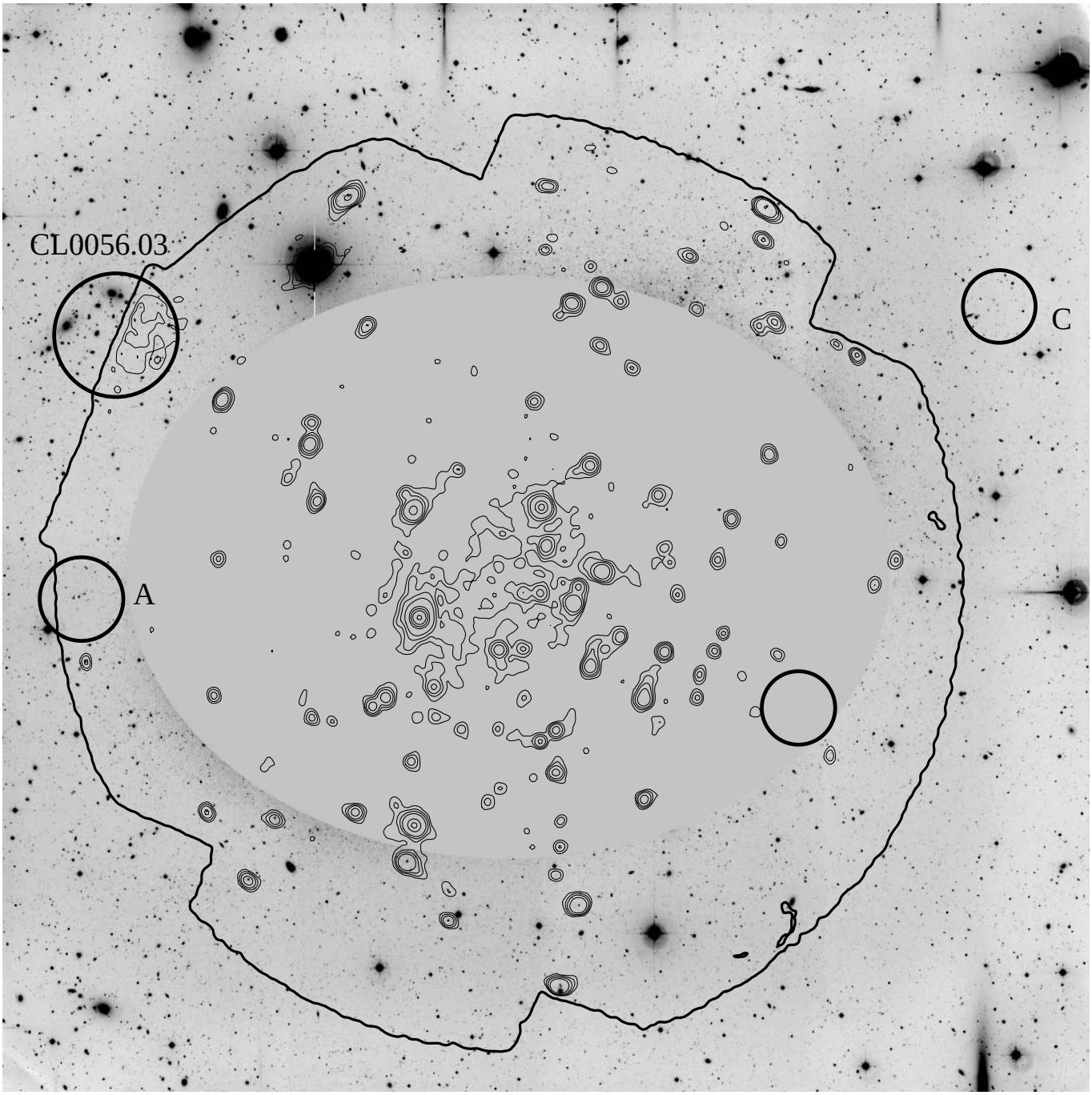

Fig. 10. A 100 ksec XMM observation of the NGC 300 field. Shown are X-ray (0.3−6.0 keV) contours and the XMM field of view, superimposed on the optical WFI data. The circles indicate the positions of CL0056.03 (upper left), clump "A" (left), clump "C" (upper right) and the $M_{\rm ap}$ peak that lies behind NGC 300 (lower right).

– Galaxies in the range [172–635] kpc of the cluster core (green triangles) show a steeper correlation with substantially larger scatter:

$$V - R = (-0.030 \pm 0.014)R + 1.376 \pm 0.264\,. \quad (14)$$

Less luminous galaxies with $R > 19$ are disproportionately bluer than those with $R < 19$, with the latter ones lying on the same sequence as the galaxies inside the innermost annulus. Fainter galaxies inside 172 kpc are bluer too, but to a much smaller extent than the galaxies in the second distance bin.

– Galaxies within 635 kpc and $R < 19$ have $V - R = 0.795 \pm 0.02$, showing no evolution.
– Galaxies in the range [635–927] kpc show no obvious concentration in colour-magnitude space, but the red sequence appears as an upper limit for the colour of those galaxies. Only two of them show significantly redder colours, whereas about a dozen appear bluer and about 20 lie on the red sequence as defined by galaxies in the inner two annuli. The upper limit indicates that a significant fraction of galaxies further away than 635 kpc could belong

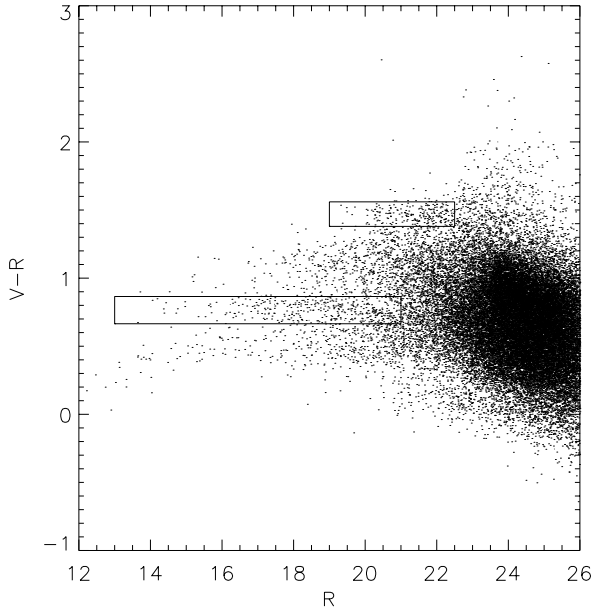

Fig. 11. The $(V-R,R)$-colour–magnitude diagram for all galaxies around NGC 300. The selected cluster sequence for CL0056.03 and CL0056.02 is marked by the large box. Besides, we checked all galaxies with $R > 23$ for spatial clustering. Only the redder objects in the upper aperture show significant clustering properties. Find more details in the text.

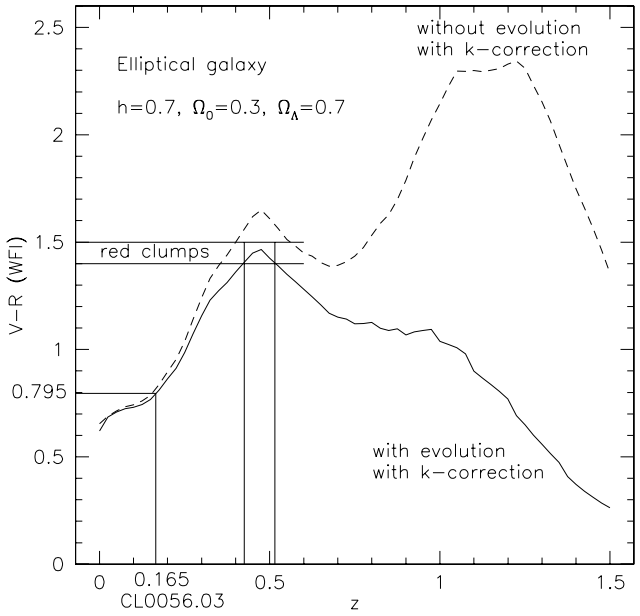

Fig. 12. Shown are predictions for the WFI@2.2 $V-R$ colours of elliptical galaxies as a function of redshift (Bolzonella et al. 2000; Bruzual & Charlot 1993). Based on the track that includes evolutionary effects we estimate the redshifts for the shear-selected red clumps.

to the cluster population. However, without any measured redshifts this fraction can not be quantified at this stage.

To summarise, for CL0056.03 a clear colour evolution for $R > 19$ and inside 635 kpc is found, increasing with the distance from the cluster core. Furthermore there exists a population of galaxies beyond 635 kpc which appears to share the same evolution limit as galaxies further inside, but they do not form a clear cluster sequence. The fraction of blue galaxies increases towards larger radii.

For CL0056.02 we find similar, but less significant results. The cluster sequence is broader and not so well-defined than the one for CL0056.03. There is no clear cut-off towards redder colours. Only galaxies inside the innermost distance bin and with $R < 19$ form a tight sequence with $V-R = 0.831 \pm 0.009$. Galaxies in the second bin have a considerably larger scatter for brighter magnitudes, but a smaller one at the faint end as compared to CL0056.03. Objects within 385 kpc show a clear colour evolution with a slope of -0.029 ± 0.019 for $R > 18.5$. Beyond 385 kpc the galaxy population becomes significantly bluer, 83% of them lie below the red sequence. The fraction of blue galaxies is larger than for CL0056.03 in the outer two annuli, whereas in the cluster cores their fraction is comparable. We note that the data quality in the field around CL0056.02 is significantly lower than for CL0056.03, increasing the photometric errors. Table 4 summarises this effect for both clusters.

Table 4. Fraction of blue galaxies. In the case of CL0056.03 a galaxy is defined to be "blue" if $V-R < 0.755$, i.e., if it lies more than 2σ below the cluster sequence $V-R = 0.795 \pm 0.02$, as defined by galaxies with $R < 19$. Galaxies with $V-R > 0.87$ are exluded from the statistics. For CL0056.02 the 2σ-threshold for "blue" galaxies is $V-R < 0.79$. Galaxies with $V-R > 0.85$ are excluded from the statistics. Note that the number of interlopers is reduced in the outer two annuli since they are significantly truncated by the edge of the field of view.

Distance from cluster centre	Galaxies with(out) z	Fraction of blue galaxies	est. No. of interlopers
CL0056.03			
0–200 kpc	11 (8)	0.26	0.6
200–740 kpc	10 (50)	0.35	6.8
740–1080 kpc	0 (34)	0.57	6.5
CL0056.02			
0–143 kpc	1 (6)	0.29	0.6
143–430 kpc	1 (26)	0.59	4.5
430–780 kpc	0 (23)	0.83	6.2

5.7. Substructure in CL0056.03

In CHM98 a velocity dispersion of 1144^{+234}_{-145}km s^{-1} is stated for CL0056.03, based on the redshifts in Table 5. From this dispersion the authors calculated a mass of $\sim 2 \times 10^{15}\ M_{\odot}$, assuming a virialised cluster and spherical symmetry. This value places CL0056.03 in the same league as supermassive clusters such as Abell 1689. Looking at Fig. 13 one notices the large elongation (∼1:4) in the distribution of the red sequence members, arguing against spherical symmetry and relaxation, in which case the virial theorem yields inaccurate results. Given the large angular separation of 105″ (300 kpc) of the two cD galaxies, we searched for a correlation between the positions of galaxies and their redshifts, indicating an ongoing merging process. The galaxies were split into two samples by drawing the perpendicular bisector of the connection line between the two cD galaxies (see left panel in Fig. 16). This way

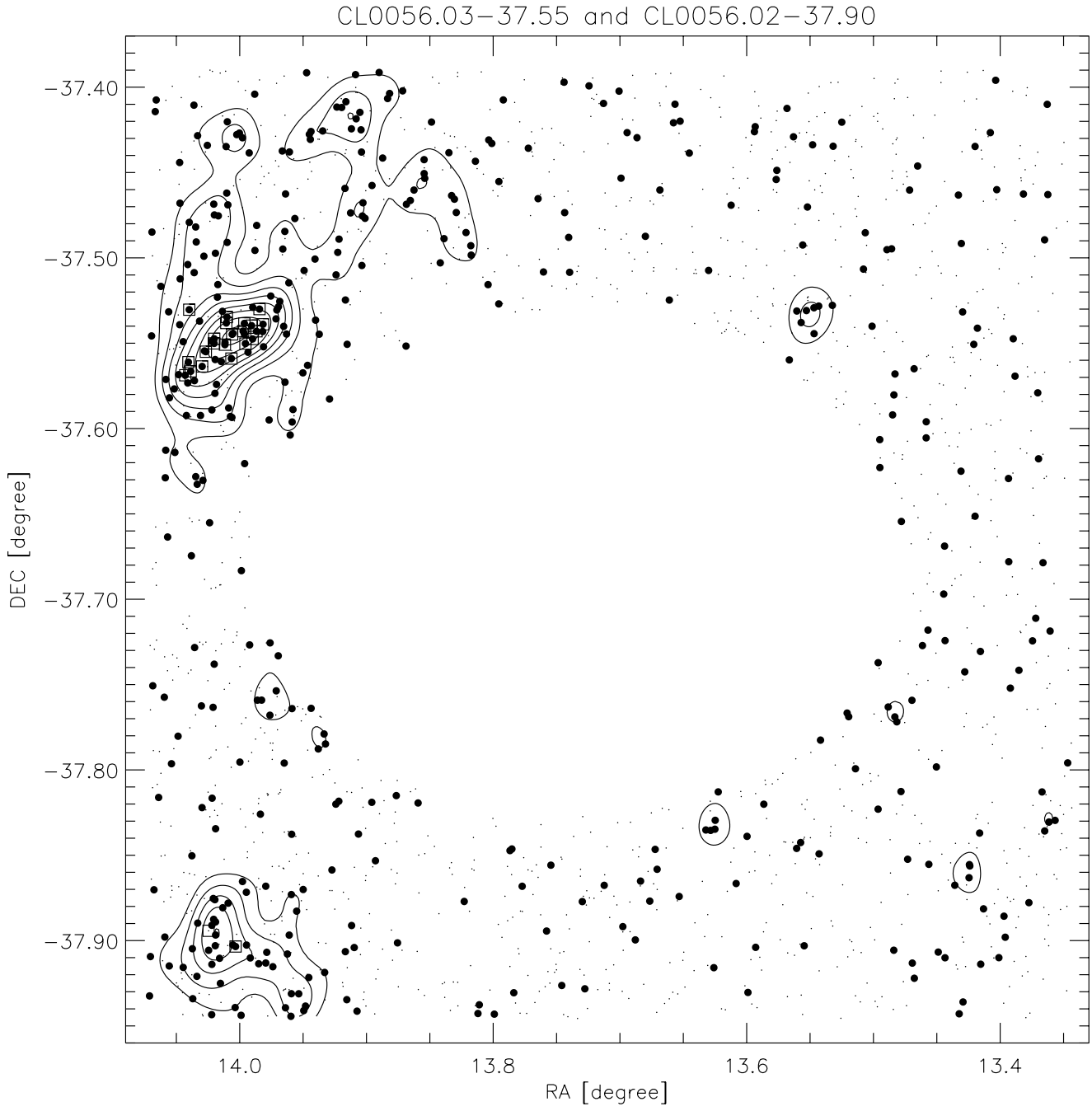

Fig. 13. Galaxies inside the lower red cluster sequence of Fig. 11 are shown as big dots. The small dots indicate galaxies brighter than $R = 21$ which do not fall inside the red sequence window. The overlaid contours are isodensity contours for the red sequence members, smoothed at a 3.′6 scale, and starting with the 1σ-overdensity contour in steps of 1σ. CL0056.03 and CL0056.02 are detected at the 8σ and 5σ level respectively. CL0056.03 appears strongly elongated, with an intersecting 12′ long filament extending north-south at its eastern side. Part of the filament could belong to Abell S0102 at $(\alpha, \delta) = (13.91, -37.41)$, a poor cluster at $z = 0.05$. Galaxies with measured spectra are highlighted with small squares around them.

10 galaxies with redshifts were assigned to the eastern cD galaxy (hereafter cD_1), and 11 to the western one (cD_2).

Figure 17 shows the redshifts of galaxies as a function of distance from the geometric cluster centre, defined as the centre of the connection line between cD_1 and cD_2. We find different mean redshifts for the galaxies around cD_1 and cD_2, translating into a velocity difference of $\sim$1824 km s^{-1}. The velocity dispersions of the two clumps are thus significantly smaller than the one given in CHM98 for the whole system, as is the total dynamical mass. Details can be found in Table 6. In order to obtain a more rigorous estimate for the significance of this discrepancy, we used Monte Carlo simulations. Galaxy redshifts were randomly distributed 10^6 times while keeping galaxy positions fixed, destroying any possible correlation between redshift and position. In only 95 out of the 10^6 cases do we find a higher mean redshift for the clump around cD_1 and a lower one

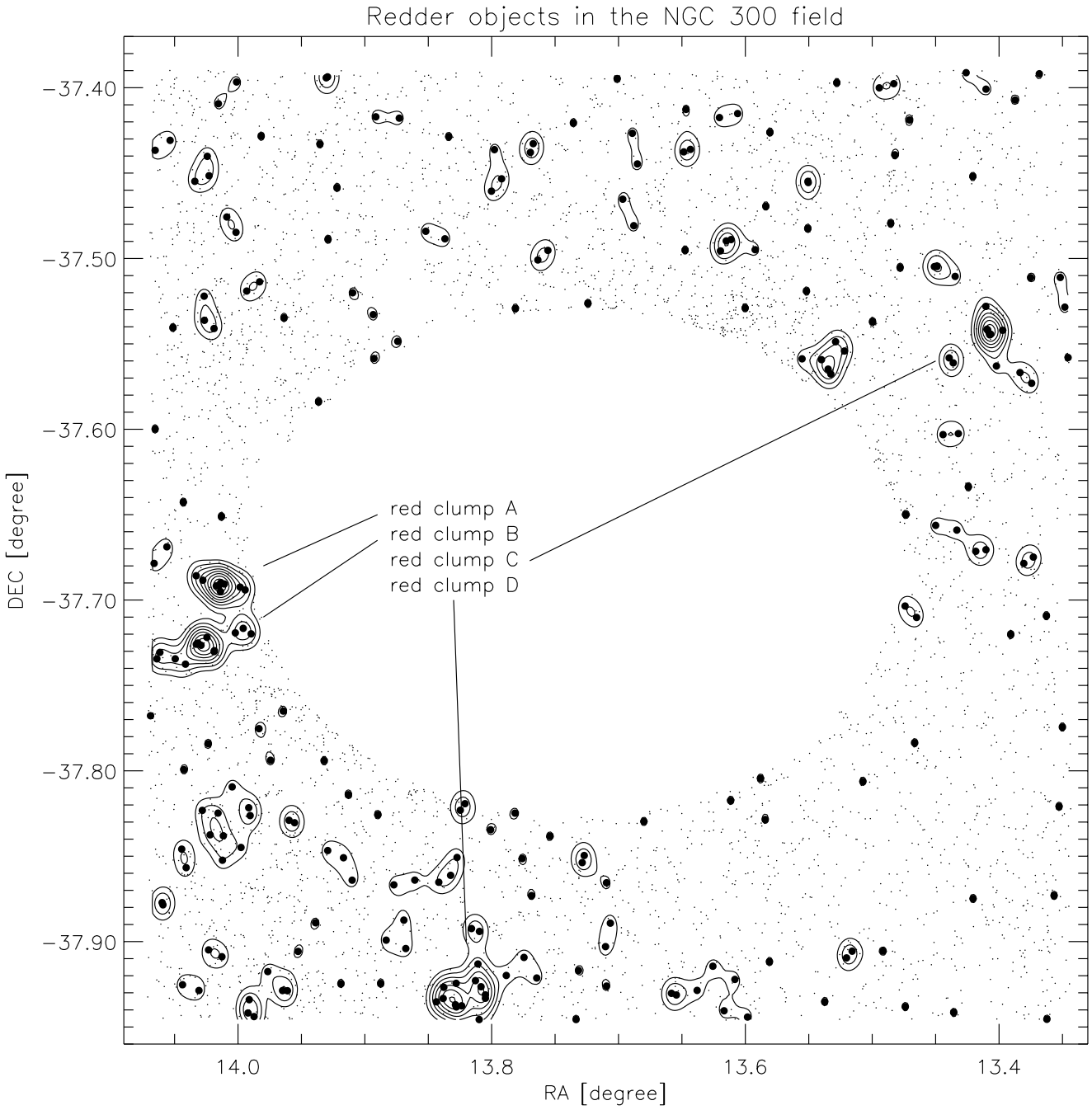

Fig. 14. Shown is the distribution of galaxies inside the upper red cluster sequence of Fig. 11 (big dots). The small dots indicate galaxies brighter than $R = 22.5$ which do not fall inside the red sequence window. Clump "A" is a very tight concentration of nine galaxies with $R < 22.3$ within 25″. There are five more galaxies spread along a 1′ filament to the east and to the west. Clump "B" is a much looser, 4′ long filament consisting of 13 galaxies without a central concentration. In the centre of the filament one finds a $R = 19.4$ bright elliptical, about 1 magnitude brighter than the second brightest member of this concentration. Clump "C" consists of 6 galaxies within 80″, the brightest one with a *R*-magnitude of 20.9. Finally, clump "D" is a very loose grouping of fainter red galaxies that looks like a chance alignment rather than a cluster. Note that the resolution of this plot is not high enough to reveal all candidate galaxies. The smoothing length for the density contours was 1.′5 arcmin. Clumps "A" and "C" lie within ∼50″ of weak lensing peaks.

for the other than in the observed data, meaning a 3.9σ significance. In addition, we checked whether the two distributions with $\sigma_{\mathrm{v},1} = 879\,\mathrm{km\,s^{-1}}$ and $\sigma_{\mathrm{v},2} = 960\,\mathrm{km\,s^{-1}}$ can be drawn from the same parent distribution with $\sigma_{\mathrm{v}} = 1296\,\mathrm{km\,s^{-1}}$. We created 10^5 random realisations of this parent Gaussian distribution, each containing 21 velocities that were ordered. Every realisation was split into two sub-samples, having the same number of overlapping objects in velocity space as the real data, shown in Fig. 17. These sub-samples contained 10 and 11 mock galaxies, and it was checked whether the difference in their mean velocities was larger than the observed $1824\,\mathrm{km\,s^{-1}}$. We found that in 96.9% of all cases the observed velocity

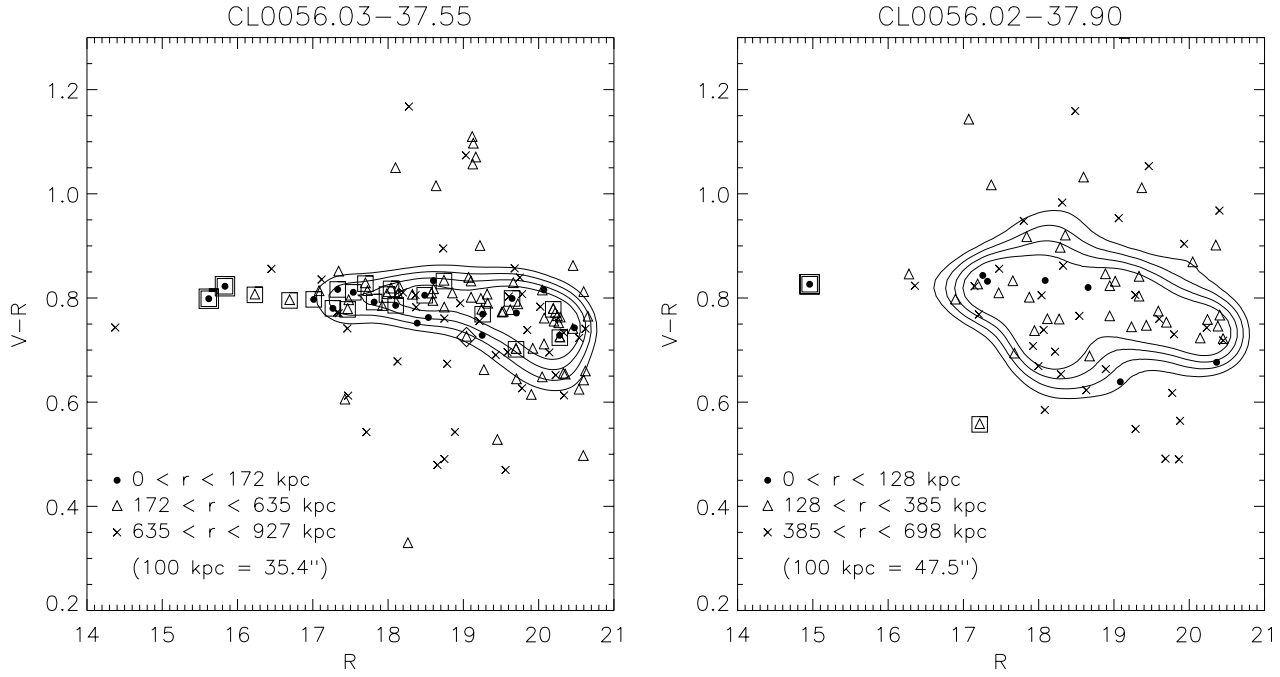

Fig. 15. Colour–magnitude diagrams for galaxies inside the cluster sequence window. Galaxies with spectroscopically determined redshifts are marked with squares, the cD galaxies are indicated with a double square (they also have measured redshifts). The galaxy with $R = 19$ and $V-R = 0.73$, marked with a diamond symbol, has $z = 0.27$, higher than the cluster redshift. Furthermore, galaxies were split into three distance bins as seen from the geometrical cluster centre. The outer radii (635 kpc respectively 385 kpc) of the second annuli were chosen in a way that galaxies in the third, outer annulus do not show an apparent concentration with respect to the red cluster sequence any more. Isodensity contours in the colour-magnitude space were calculated from all galaxies.

Table 5. Heliocentric redshifts for CL0056.03, taken from CHM98. Here, v denotes the radial velocity in km s^{-1} together with its measurement errors σ_v, and the index m indicates whether a galaxy is closer to the eastern cD galaxy (ID = 6), or to the western one (ID = 16).

ID	RA (2000.0)	DEC (2000.0)	v	σ_v	z	m
1	00:56:10.23	–37:34:07.9	51570	282	0.17202	1
2	00:56:09.22	–37:33:59.5	50799	51	0.16945	1
3	00:56:07.07	–37:33:49.4	51628	138	0.17221	1
4	00:56:09.71	–37:33:39.9	50709	120	0.16915	1
5	00:56:01.49	–37:33:31.6	49315	111	0.16450	1
6	00:56:06.41	–37:33:18.0	49754	154	0.16596	cD 1
7	00:55:57.50	–37:32:51.5	46839	38	0.15624	2
8	00:55:58.90	–37:33:00.7	48490	50	0.16175	2
9	00:56:02.76	–37:33:03.9	49588	192	0.16541	1
10	00:56:04.76	–37:33:00.3	50394	117	0.16810	1
11	00:56:04.75	–37:32:51.0	51594	84	0.17210	1
12	00:55:55.59	–37:32:20.2	48514	145	0.16183	2
13	00:55:56.74	–37:32:35.4	49555	123	0.16530	2
14	00:55:57.74	–37:32:23.4	48256	101	0.16096	2
15	00:55:59.32	–37:32:35.2	49041	145	0.16358	2
16	00:55:59.09	–37:32:18.2	48888	117	0.16307	cD 2
17	00:56:01.32	–37:32:41.9	50168	187	0.16734	2
18	00:56:02.45	–37:32:18.0	47381	138	0.15805	2
19	00:56:02.41	–37:32:05.7	49097	113	0.16377	2
20	00:55:56.18	–37:31:48.3	49439	14	0.16491	2
21	00:56:09.54	–37:31:49.0	49863	107	0.16633	1

histogram could not be drawn from a single Gaussian distribution, thus the clumps probably did not yet mix.

We note that the velocity difference between cD_1 and cD_2 themselves, however, is $v = 866\,\mathrm{km\,s^{-1}}$ and thus much lower than the difference between the sub-clumps. We conclude that

Table 6. Properties for the eastern and western clumps around cD_1 respectively cD_2.

Clump	$\langle z \rangle$	$\langle v \rangle$ [km s^{-1}]	σ_v [km s^{-1}]
cD_1	0.1685 ± 0.0029	50521	879
cD_2	0.1624 ± 0.0032	48697	960

the 21 measured redshifts for CL0056.03 are probably not representative for the ∼113 cluster member candidates, as identified by their colours.

In the following a simple dynamical model is used in order to check whether the system is gravitationally bound or unbound. A linear orbit of the clumps is assumed, i.e. there is no shear or rotation component. The system is seen under some inclination angle φ, with $\varphi = 0$ if the clumps were aligned along the line of sight. Based on Newtonian dynamics the condition of a bound system can be written as $v^2 r \le 2GM$, or, taking into account the inclination angle φ, as

$$\frac{v_\mathrm{r}^2 r_\mathrm{p}}{2GM} \le \sin^2\varphi \cos\varphi, \tag{15}$$

where $v_\mathrm{r} = 1824\,\mathrm{km\,s^{-1}}$ is the radial velocity difference between the clumps and $r_\mathrm{p} = 300\,\mathrm{kpc}$ the projected distance on the sky between cD_1 and cD_2. M is the total mass of the system. The right hand side of (15) can not get larger than 0.385 for $\varphi = 54°$. For $M \le 3.0 \times 10^{14}\,M_\odot$ the expression (15) does not allow bound solutions for the given v_r and r_p.

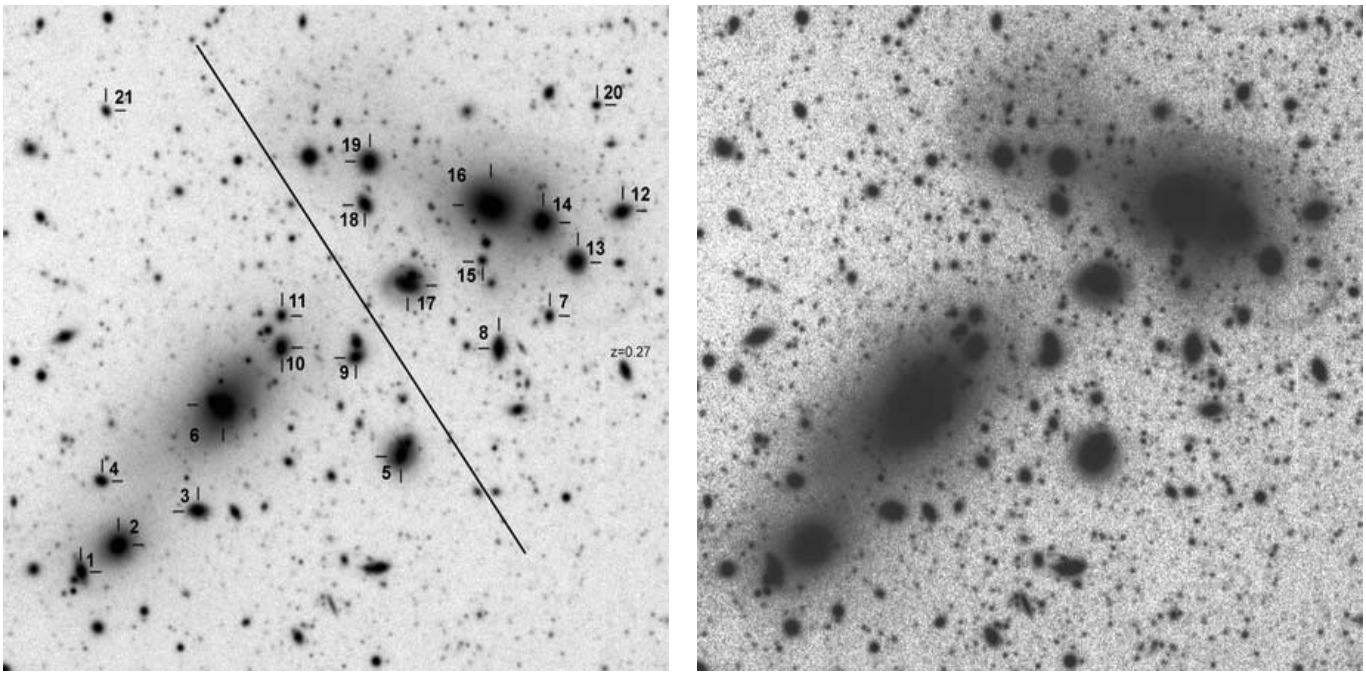

Fig. 16. Image of CL0056.03. In the left panel the 21 spectroscopically confirmed cluster members are shown, together with the perpendicular bisector of the connection line between the two cD galaxies, which we chose to split the cluster galaxies into two samples. An [OII] emission line galaxy at higher redshift is indicated. The right panel shows a steeper scaled version of the image at left, showing that cD_1 and cD_2 are both embedded in large, but well separated haloes.

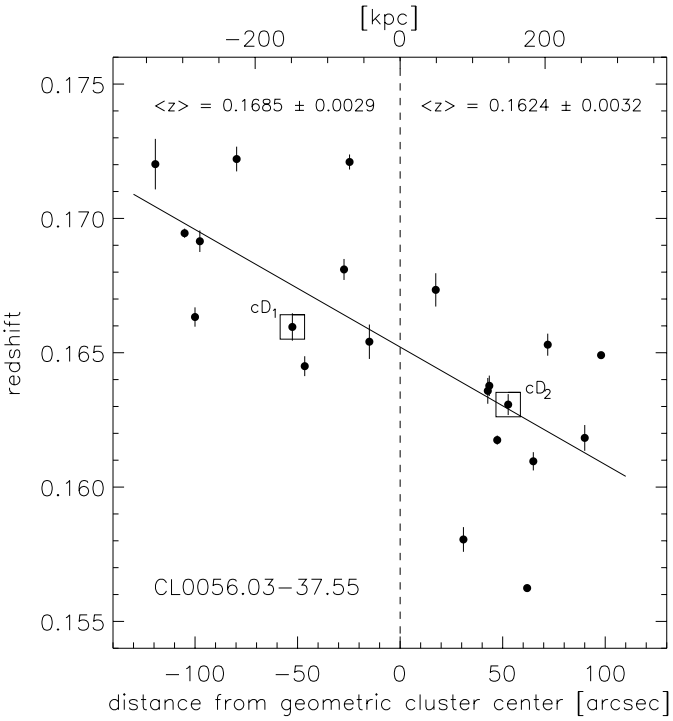

Fig. 17. The redshifts of the galaxies in CL0056.03 as a function of distance from the geometrical cluster centre. There is a highly significant (~4σ) correlation between galaxy position and redshift, indicating that CL0056.03 actually consists of two possibly merging subclumps. The slope of the linear fit is different from zero on the 4.1σ level. Note that cD_1 has a peculiar motion of 780 km s^{-1} with respect to its own clump.

For $M = 5.0 \times 10^{14}\,M_\odot$ the probability for a bound system is 49% (the fraction of allowed inclination angles over all inclination angles), and it increases to 70% for $M = 1.0 \times 10^{15}\,M_\odot$. Thus, the lensing estimated mass of $M = 1.4 \times 10^{14}\,M_\odot$ for CL0056.03 is not sufficient for a bound solution. If the velocity difference $v_r = 866\,\mathrm{km\,s^{-1}}$ between the two most luminous galaxies cD_1 and cD_2 was representative for CL0056.03, instead, then in 57% of the cases the system would be gravitationally bound.

Our interpretation for the dynamical state of CL0056.03 is thus that the eastern clump is closer to us and the western one further away, and that the system is in a pre-collision phase with the two clumps approaching each other, since probably no mixing has yet taken place. In addition, there is some indication from the imaging data itself, arguing for this scenario: both the eastern and the western clump are embedded in large, but well separated haloes, each measuring about 340 kpc. The halo around the western clump, in particular, shows tidal features. We take this as an evidence for ongoing tidal stripping and merging processes inside the clumps, but probably no encounter has yet taken place between them. In the spectra taken by CHM98 no emission lines are found for the cluster members, thus there is no sign for nuclear activity or major star formation. The other scenario is that there was already an encounter and the two clumps are receding, which would place the western clump closer to the observer. Based on the small number of spectra the latter state can not be ruled out.

Besides the two sub-clumps there is some evidence for a more extended structure in CL0056.03. In Fig. 13 a filament is seen, extending to about 7′ north and 4′ south of the cluster centre, but not lined up with the cluster centre itself. The angle

between this linear filament and the orientation of CL0056.03 is ∼40 degrees. North of CL0056.03 at (α = 00:55:45.6, δ = −37:24:46), however, the small cluster Abell S0102 is found at a redshift of $z = 0.056$. A contamination of the possible filament by member galaxies of Abell S0102 cannot be ruled out. Furthermore, 5′.2 from the cluster centre and in the direction of the cluster orientation, an isolated elliptical galaxy with $R = 14.4$ and $V - R = 0.745$ is found, 0.05 mag bluer than the cluster sequence. Its distance to the centre of Abell S0102 is 6′.2. Based on the present data it cannot be concluded whether this elliptical is isolated in space or a physical member at the fringes of one of the two clusters.

6. Conclusion

We introduced the Garching-Bonn Deep Survey, a 12 square degree survey for weak lensing investigations. It is primarily a "virtual" survey, since about 75% of the data was taken from the ESO archive. Within a dedicated ASTROVIRTEL program the functionality of the *querator* search engine was substantially expanded. It now allows an effective filtering of the data with respect to characteristic properties. One of these archival fields, centreed on NGC 300, showed two concentrations of background galaxies upon visual inspection of the field in the DSS. The cluster nature of these two concentrations was spectroscopically confirmed beforehand by other groups.

Making use of the high quality of the *R*-band exposures, we showed that one of the two clusters (CL0056.03) can be detected by its weak gravitational shear signal. The second cluster (CL0056.02) was not found in the weak lensing data, probably due to field truncation and insufficient image quality. Besides, two other significant and coherent shear patterns were detected. Both of them coincide with significant overdensities of red galaxies, for which we gave redshift and mass estimates, based on their apparent colour and lensing strength. A third shear detection was seen behind NGC 300 itself, but there is no further evidence from background light for a cluster of galaxies at this position. Thus, apart from this hidden detection, all $M_{\rm ap}$ peaks equal to or higher than 3σ in filter scales ≥3′.2 coincide with overdensities of red galaxies. These $M_{\rm ap}$ peaks, however, are at the limit of what can be concluded from this data set. The tidal gravitational fields of more massive clusters of galaxies imprint shear fields in the images of background galaxies that are easily detected on the 10σ level and beyond (Clowe & Schneider 2002).

Based on the high virial mass of CL0056.03, derived from spectroscopic data by CHM98, and the comparatively shallow weak lensing signal, a closer analysis of this cluster was performed. A highly significant correlation between redshift and the position of galaxies in the cluster is found, indicating the existence of two sub-clumps, separated by 1824 km s^{-1} in velocity space. Based on the present data and the derived lensing mass it cannot be concluded whether the system is gravitationally bound. By looking at the projected sky distribution of galaxies with similar properties in a $(V - R, R)$ colour–magnitude diagram, we find an extended filament of galaxies inclined to the cluster's major axis. Without further spectroscopic data of galaxies in this filament its nature can not be further clearified. We take the presented properties as evidence that CL0056.03 is a younger cluster in formation and has not yet reached its equilibrium state.

CL0056.03 shows a clear and tight red sequence in the $(V - R, R)$ colour-magnitude space, with an increasing fraction of bluer galaxies towards larger cluster radii. CL0056.02 also shows a red sequence, the results presented for this cluster, however, are more uncertain due to field truncation and inferior data quality.

Acknowledgements. The authors thank Nathalie Fourniol and Benoit Pirenne (ESO archive), for their excellent assistance of our frequent and substantial data requests. Furthermore the kind provision of *FLIPS* by Jean-Charles Cuillandre is greatly appreciated. MS thanks Matthias Bartelmann, Oliver Czoske, Evanthia Hatziminaoglou, Lindsay King, Joan-Marc Miralles and Stella Seitz for providing photometric redshift estimates, further discussions and many corrections. WG and GP gratefully acknowledge support for this research from the Chilean Center for Astrophysics FONDAP 15010003. SC was supported by the German Ministry for Science and Education (BMBF) under the grant number 50OX0002. The support given by ASTROVIRTEL, a Project funded by the European Commission under FP5 Contract No. HPRI-CT-1999-00081, is acknowledged. This work was furthermore supported by the BMBF through the DLR under the project 50 OR 0106, by the BMBF through DESY under the project 05AE2PDA/8, and by the Deutsche Forschungsgemeinschaft (DFG) under the project SCHN 342/3–1.

References

Bacon, D. J., Refregier, A. R., & Ellis, R. S. 2000, MNRAS, 318, 625
Bacon, D. J., Massey, R., Refregier, A., & Ellis, R. S. 2002 [astro-ph/0203134]
Bartelmann, M., & Schneider, P. 2001, Phys. Rep., 340, 291
Bertin, E., & Arnouts, S. 1996, A&AS, 117, 393
Bolzonella, M., Miralles, J. M., & Pelló, R. 2000, A&A, 363, 476
Brainerd, T., Blandford, R. D., & Smail, I. 1996, ApJ, 466, 623
Bruzual, A. G., & Charlot, S. 1993, ApJ, 405, 538
Cappi, A., Held, E. V., & Marano, B. 1998, A&AS, 129, 31
Clowe, D., & Schneider, P. 2002, A&A, 395, 385
Collins, C. A., Guzzo, L., Nichol, R. C., & Lumsden, S. L. 1995, MNRAS, 274, 1071
Dahle, H., Pedersen, K., Lilje, P. B., Maddox, S. J., & Kaiser, N. 2002 [astro-ph/0208050]
Dannerbauer, H., Lehnert, M. D., Lutz, D., et al. 2002, ApJ, 573, 473
Erben, T., van Waerbeke, L., Mellier, Y., et al. 2000, A&A, 355, 23
Erben, T., van Waerbeke, L., Bertin, E., Mellier, Y., & Schneider, P. 2001, A&A, 336, 717
Freedman, W. L., Madore, B. F., Gibson, B. K., et al. 2001, ApJ, 553, 47
Gladder, M. D., & Yee, H. K. C. 2000, AJ, 120, 2148
Greisen, E. W., & Calabretta, M. R. 2002, A&A, 395, 1061
Jain, B., & van Waerbeke, L. 2000, ApJ, 530, L1
Kaiser, N., Wilson, G., & Luppino, G. A. 2000 [astro-ph/0003338]
Kaiser, N., Squires, G., & Broadhurst, T. 1995, AJ, 449, 460
Kruse, G., & Schneider, P. 1999, MNRAS, 302, 821
Kruse, G., & Schneider, P. 2000, MNRAS, 318, 321
Maoli, R., van Waerbeke, L., Mellier, Y., et al. 2001, A&A, 368, 766
Margoniner, V. E., & Deep Lens Survey Team 2003 [astro-ph/0303381]

Mellier, Y. 1999, ARA&A, 37, 127
Miralles, J. M., Erben, T., Hämmerle, H., et al. 2002, A&A, 388, 68
Miyazaki, S., Hamana, T., Shimasaku, K., et al. 2002, ApJ, 580, 97
Navarro, J., Frenk, C., & White, S. 1996, ApJ, 642, 563
Pierfederici, F. 2001, Proc. SPIE, 4477, 246
Pietrzynski, G., Gieren, W., Fouqué, P., & Pont, F. 2002a, AJ, 123, 789
Pietrzynski, G., Gieren, W., & Udalski, A. 2002b, PASP, 114, 298
Read, A. M., & Pietsch, W. 2001, A&A, 373, 473
Schneider, P. 1996, MNRAS, 283, 837
Umetsu, K., & Futamase, T. 2000, ApJ, 539, L5
van Waerbeke, L., Mellier, Y., Radovich, M., et al. 2001, A&A, 374, 757
van Waerbeke, L., Mellier, Y., Erben, T., et al. 2000, A&A, 358, 30
Voges, W., Aschenbach, B., Boller, T., et al. 1999, A&A, 349, 389
Wittman, D., Tyson, J. A., Margoniner, V. E., et al. 2001, ApJ, 557, 89
Wittman, D., Margoniner, V. E., & Tyson, J. A. 2002 [astro-ph/0210120]
Wittman, D., Tyson, J. A., Kirkman, D., Dell'Antonio, I., & Bernstein, G. 2000, Nature, 405, 143